Effects of wall vibrations on channel flows

N.N. Haq[1] and J.M. Floryan[1],†

[1]Department of Mechanical and Materials Engineering, The University of Western Ontario, London, ON N6A 5B9, Canada

The effect of surface vibrations on the pressure-gradient-driven flows in channels has been studied. The analysis considered monochromatic waves and laminar flows. The effectiveness of the vibrations was gauged by determining the pressure gradient correction required to maintain the same flow rate as without vibrations. Waves propagating upstream always increase pressure losses. Flow response to waves propagating downstream is more complex and changes as a function of the flow Reynolds number. Such waves reduce losses if the Reynolds number $Re < \sim100$, but these waves must be sufficiently fast to reduce pressure losses for larger Re values. In general, the supercritical waves, i.e. waves faster than the reference flow, reduce pressure losses with the magnitude of reduction increasing monotonically with the wave phase speed and wavenumber. The need for an external pressure gradient is eliminated if sufficiently short and fast waves are used. Generally, the subcritical waves, i.e. waves with velocities similar to the reference flow, increase pressure losses. This increase changes somewhat irregularly as a function of the wave phase speed and wavenumber forming local maxima and minima. These waves can reduce pressure losses only if the Reynolds number becomes large enough. It is shown that subcritical waves with very small amplitudes but matching the natural flow frequencies produce significant pressure losses.

Key words: control theory, drag reduction

1. Introduction

Fluid transportation through conduits relies on a pressure gradient to overcome frictional resistance. Finding means for its reduction is economically significant as it translates into considerable energy savings (Beiler *et al.* 2006; Spalart & McLean 2011). Classical methods rely on creating a pressure difference between the inlet and outlet, but the magnitude of this difference is limited by the available technology, which places an upper limit on the system's performance. This limitation led to a search for techniques that either

† Email address for correspondence: floryan@uwo.ca

reduce frictional resistance or provide a method to augment propulsion (Hoepffner & Fukagata 2009). Surface vibrations offer potential which could be used to achieve either of these goals.

Spatial flow modifications have been extensively explored in the search for the reduction of frictional resistance. The existing strategies can be divided into three groups. Prevention of the onset of the laminar–turbulent transition represents the first group, with the leading question being if a modulated laminar flow is more stable than an unmodulated flow. The second group involves flow relaminarization. Search for spatial modulations that can directly reduce frictional drag represents the third group. Work in this area resulted in a large body of literature devoted to modulating turbulent flows. Literature on modulations of laminar flows, which are of interest here, is not well developed.

Several studies have demonstrated the ability to achieve drag reduction in smooth channels when using modulations created by wall transpiration (Min *et al.* 2006; Mamori, Iwamoto & Murata 2014; Gómez *et al.* 2016; Han & Huang 2020; Jiao & Floryan 2021*a*,*b*) even attaining sustained sub-laminar levels of drag (Min *et al.* 2006; Jiao & Floryan 2021*a*,*b*). Bewley (2009) and Fukagata, Sugiyama & Kasagi (2009) provided a partial answer regarding the net energetic benefit of transpiration applied to smooth surfaces, i.e. they demonstrated that the net energy reduction could not be achieved as the energy cost of transpiration consistently exceeds the energy gain due to drag reduction. Recent results show that combining different forms of modulation, e.g. adding in-plane wall oscillations, can save net energy (Floryan 2023). It is known that transpiration activates nonlinear drift, which can be used for propulsion augmentation (Jiao & Floryan 2021*a*,*b*). Analysis of flows bounded by non-smooth surfaces shows a reduction of frictional drag in laminar (Mohammadi & Floryan 2013*a*,*b*; Yadav, Gepner & Szumbarski 2021; Moradi & Floryan 2013) and turbulent (Walsh 1983; Chen *et al.* 2016) flows if a proper surface topography is used. Fukagata *et al.* (2009) raised the possibility that transpiration in a duct with varying cross-sectional shapes may reduce net energy requirements, although this has yet to be demonstrated.

A large volume of numerical and experimental works aiming at friction reduction in turbulent flows involved modulations created by spanwise wall oscillations – see recent reviews by Leschziner (2020) and Ricco, Skote & Leschziner (2021). Direct numerical simulations showed that gross drag for various geometries and combinations of flow parameters could be reduced by 30–40%, with up to 50% of this reduction driven by the 'pumping' action of travelling waves of the wall spanwise velocity (Quadrio & Ricco 2004; Hurst, Yang & Chung 2014). The mechanisms responsible for drag reduction are based on interference with near-wall turbulence, with different authors stressing different elements of this interference (Gatti & Quadrio 2016). Subtraction of actuation power resulted in net power savings of no more than 10% (Quadrio, Ricco & Viotti 2009; Gatti & Quadrio 2016). Obviously, the near-wall turbulence needs to be re-arranged by active or passive action to reduce shear, but it remains to be determined how to achieve that practically and efficiently.

Recent analyses of structured convection demonstrated its ability to reduce pressure losses significantly in low-Reynolds-number flows. Heating modulations create separation bubbles that limit the direct contact between the stream and the bounding wall, thereby reducing wall shear. The variable-density-driven motion within the bubbles provides additional propulsion (Hossain, Floryan & Floryan 2012; Floryan & Floryan 2015; Hossain & Floryan 2016; Inasawa, Taneda & Floryan 2019). The modified temperature field may induce a net buoyancy force which may either assist or oppose the pressure gradient (Floryan, Wang & Bassom 2023*a*). Using heated grooves may amplify this effect if heating and grooves patterns are placed correctly (Hossain & Floryan 2020). New effects which

can be used to provide propulsion assistance include thermal drift (Abtahi & Floryan 2017; Inasawa, Hara & Floryan 2021) and pattern interaction (Floryan & Inasawa 2021).

The literature on the effect of transverse wall motions is mainly focused on travelling waves as they activate the peristaltic effect, whose essential features are well known (Jaffrin & Shapiro 1971). The available literature deals mainly with biological systems where analysis of the Stokes approximation for long and slow waves is relevant (Lauga 2016); see a recent review by Ali, Ullah & Rasool (2020). The first complete analysis of fast waves was given very recently (Floryan, Faisal & Panday 2021) and extended to propulsion augmentation (Haq & Floryan 2022) and resistance reduction (Floryan & Zandi 2019; Floryan & Haq 2022). There is a lack of a systematic analysis of flows in a channel with vibrating walls and identification of different flow regimes, especially from the resistance reduction point of view.

Analysis of vibrations requires repeated solutions of an unsteady moving boundary problem to assess the effects of different types of waves. This analysis concerns sustained vibrations, which make Eulerian algorithms preferable (Floryan & Rasmussen 1989). Typical Eulerian methods use low-order spatial discretization schemes combined with various boundary-tracking procedures. One group of these procedures requires boundary reconstruction at each time step resulting in the smearing of its location and thus is not suitable for this analysis. Another group requires numerical construction of boundary-conforming grids, which is time-consuming and suffers from accuracy problems. There are unique, high-accuracy grid generation methods (Floryan 1985, 1986; Floryan & Zemach 1987, 1993), but their implementation is cumbersome. There are also domain transformation methods that bypass grid generation but result in very complex forms of equations (Cabal, Szumbarski & Floryan 2001, 2002). This analysis requires an accurate algorithm that handles multiple geometries with little labour overhead. This led to the selection of the spectrally accurate immersed boundary conditions (IBC) method, whose details can be found in Szumbarski & Floryan (1999), Husain & Floryan (2008*a*,*b*, 2010) and Husain, Szumbarski & Floryan (2009).

This analysis concerns laminar pressure gradient-driven flows with Poiseuille flow representing the reference configuration. The characteristic properties of this flow are the parabolic velocity distribution and a linear stability limit at $Re = 5772.22$ (Orszag 1971). Various routes to secondary states, as well as to turbulence, are summarized by Schmid & Henningson (2001). Bypass routes to transition can be initiated by introducing spatial flow modulations using wall transpiration (Floryan 1997), adding transverse ribs (Floryan 2005, 2007) and adding longitudinal grooves (Mohammadi & Floryan 2013*a*,*b*), among others.

This study's main objective is to characterize flow modifications induced by vibrations in the pressure-gradient-driven laminar channel flow and assess their ability to affect pressure losses. The secondary objective is to identify conditions which may lead to a more intense mixing; this is manifested by increase of pressure losses. Section 2 describes the model problem used in the analysis. Section 3 explains the solution method. Section 4 briefly summarizes the properties of the peristaltic effect. Vibration-induced modifications of the velocity field are presented in § 5. Section 6 is devoted to a discussion of pressure losses. In particular, §§ 6.1, 6.2 and 6.3 deal with small-, medium- and large-Reynolds-number flow, respectively. Presentation in § 6.3 is divided into a discussion of supercritical waves (§ 6.3.1), subcritical waves away from resonance (§ 6.3.2), subcritical waves near resonance (§ 6.3.3) and the effect of critical layers (§ 6.3.4). Section 7 provides a summary of the main results. Additional information is provided in the appendices – Appendix A offers an analytic solution for long-wavelength
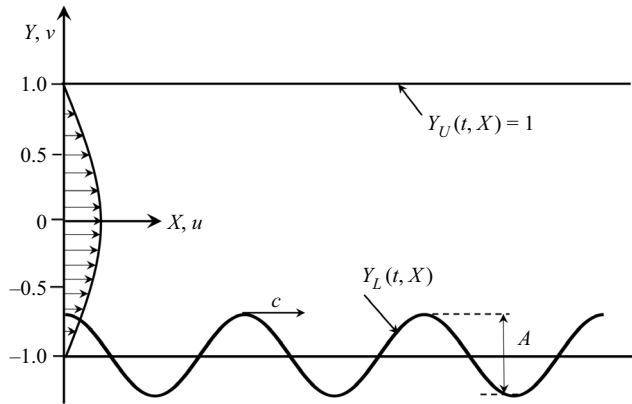
Figure 1. Sketch of the flow configuration.

vibrations, Appendix B presents an analytic solution for small amplitude waves and Appendix C explains the method of determining the natural flow frequencies.

2. Problem formulation

Consider the steady, two-dimensional flow of a fluid confined in a channel bounded by two parallel walls extending to $\pm\infty$ in the X-direction. The plates are placed at a distance $2h$ apart (see figure 1), the flow is driven in the positive X-direction by a pressure gradient resulting in the velocity and pressure fields, and the flow rate of the form

$$\boldsymbol{v}_0(X, Y) = (1 - Y^2, 0), \quad p_0(X, Y) = -2X/Re, \quad \Psi_0 = Y - \frac{Y^3}{3} + \frac{2}{3}, \quad Q_0 = \frac{4}{3},$$
(2.1a–d)

where $\boldsymbol{v}_0 = (u_0, v_0)$ denotes the velocity vector scaled with the maximum of the X-velocity u_{max}; p_0 stands for the pressure scaled with ρu_{max}^2, where ρ stands for the density; Ψ_0 stands for the stream function; Q_0 denotes the flow rate; the Reynolds number is defined as $Re = u_{max}h/\nu$, where ν stands for the kinematic viscosity; and h has been used as the length scale. The flow is modified by imposing wall vibrations as travelling waves with known amplitudes. The waves propagate along the channel axis while material points at the wall move only in the transverse direction (they do not move along the channel axis). The resulting time-dependent channel geometry is described as

$$Y_U(t, X) = 1, \quad Y_L(t, X) = -1 + \tfrac{1}{2}A \cos[\alpha(X - ct)],$$
(2.2a,b)

where subscripts U and L refer to the upper and lower walls.

Surface vibrations affect the flow field, which we shall represent as a sum of the reference flow and the vibration-induced modifications, i.e.

$$u(t, X, Y) = Re\, u_0(Y) + u_1(t, X, Y), \quad v(t, X, Y) = v_1(t, X, Y),$$
(2.3a,b)

$$p(t, X, Y) = Re^2 p_0(X) - B_{mod}X + p_1(t, X, Y), \quad \psi(t, X, Y) = Re\, \psi_0(Y) + \psi_1(t, X, Y).$$
(2.3c,d)

In the above, (u, v), p, ψ denote the complete velocity, pressure and stream function, respectively, and (u_1, v_1) and ψ_1 denote the velocity and stream function modifications,

968 A8-4

respectively, B_{mod} stands for the pressure gradient correction associated with modifications with negative B_{mod} signalling reduction of pressure losses, and p_1 denotes the periodic part of pressure field modifications. Substitution of (2.3) into the Navier–Stokes and continuity equations leads to the field equations for the flow modifications of the form

$$\frac{\partial u_1}{\partial t} + (Re\, u_0 + u_1)\frac{\partial u_1}{\partial X} + Re\, v_1 \frac{du_0}{dY} + v_1 \frac{\partial u_1}{\partial Y} = B_{mod} - \frac{\partial p_1}{\partial X} + \frac{\partial^2 u_1}{\partial X^2} + \frac{\partial^2 u_1}{\partial Y^2}, \quad (2.4a)$$

$$\frac{\partial v_1}{\partial t} + (Re\, u_0 + u_1)\frac{\partial v_1}{\partial X} + v_1 \frac{\partial v_1}{\partial Y} = -\frac{\partial p_1}{\partial Y} + \frac{\partial^2 v_1}{\partial X^2} + \frac{\partial^2 v_1}{\partial Y^2}, \quad (2.4b)$$

$$\frac{\partial u_1}{\partial X} + \frac{\partial v_1}{\partial Y} = 0, \quad (2.4c)$$

subject to boundary conditions of the form

$$u_1(t, X, 1) = 0, \quad v_1(t, X, 1) = 0, \quad (2.4d)$$

$$u_1(t, X, Y_L(t, X)) = -Re\, u_0(Y_L(t, X)), \quad v_1(t, X, Y_L(t, X)) = \tfrac{1}{2}c\,\alpha A \sin[\alpha(X - ct)], \quad (2.4e)$$

where (u_1, v_1) denote the components of the modification velocity vector in the (X, Y)-directions scaled with $U_v = \nu/h$ as the velocity scale, p_1 denotes pressure scaled with ρU_v^2 as the pressure scale and t stands for time scaled with h/U_v as the time scale. We are interested in determining if surface vibrations can reduce the pressure gradient required to maintain the specified flow rate. Accordingly, we impose the mass flow rate constraint of the form

$$Q = Q(t, X)|_{mean} = \left(\int_{Y_L(t,X)}^{1} u(t, X, Y)\, dY\right)\bigg|_{mean} = \frac{4}{3}Re. \quad (2.4f)$$

The subscript 'mean' refers to the average over one time period. Description of the flow mechanics requires knowledge of surface forces acting on the fluid at the walls. We begin with the lower wall and start with the determination of the stress vector $\boldsymbol{\sigma}_L$,

$$\boldsymbol{\sigma}_L = [\sigma_{X,L} \quad \sigma_{Y,L}] = [n_{X,L} \quad n_{Y,L}]\begin{bmatrix} 2\dfrac{\partial u_1}{\partial X} - p & Re\dfrac{du_0}{dY} + \dfrac{\partial u_1}{\partial Y} + \dfrac{\partial v_1}{\partial X} \\ Re\dfrac{du_0}{dY} + \dfrac{\partial u_1}{\partial Y} + \dfrac{\partial v_1}{\partial X} & 2\dfrac{\partial v_1}{\partial Y} - p \end{bmatrix}_{Y=Y_L}, \quad (2.5)$$

where the normal unit vector $\boldsymbol{n}_L$ pointing outwards is expressed as

$$\boldsymbol{n}_L = [\, n_{X,L} \quad n_{Y,L} \,] = N_L\left(\frac{\partial Y_L}{\partial X}, \ -1\right), \quad N_L = \left[1 + \left(\frac{\partial Y_L}{\partial X}\right)^2\right]^{-1/2}. \quad (2.6)$$

The components of the stress vector are written as

$$\sigma_{X,L} = \sigma_{Xv,L} + \sigma_{Xp,L} = N_L\left[2\frac{\partial Y_L}{\partial X}\frac{\partial u_1}{\partial X}\bigg|_{Y_L} - \left(Re\frac{du_0}{dY} + \frac{\partial u_1}{\partial Y} + \frac{\partial v_1}{\partial X}\right)\bigg|_{Y_L}\right] - N_L\frac{\partial Y_L}{\partial X}p\bigg|_{Y_L}, \quad (2.7a)$$

$$\sigma_{Y,L} = \sigma_{Yv,L} + \sigma_{Yp,L} = N_L\left[\frac{\partial Y_L}{\partial X}\left(Re\frac{du_0}{dY} + \frac{\partial u_1}{\partial Y} + \frac{\partial v_1}{\partial X}\right)\bigg|_{Y_L} - 2\frac{\partial v_1}{\partial Y}\bigg|_{Y_L}\right] + N_L\, p|_{Y_L}, \quad (2.7b)$$

968 A8-5

where $(\sigma_{Xv,L}, \sigma_{Yv,L})$ and $(\sigma_{Xp,L}, \sigma_{Yp,L})$ denote the viscous and pressure contributions, respectively. The X- and Y-components of the total force $(F_{X,L}, F_{Y,L})$ (per unit length along the channel and unit width of the channel) are expressed as

$$F_{X,L} = F_{Xv,L} + F_{Xp,L} = \lambda^{-1} \int_{X_0}^{X_0+\lambda} \left[2 \frac{\partial Y_L}{\partial X} \frac{\partial u_1}{\partial X} \bigg|_{y_L} - \left(Re \frac{du_0}{dY} + \frac{\partial u_1}{\partial Y} + \frac{\partial v_1}{\partial X} \right) \bigg|_{Y_L} \right] dX$$

$$- \lambda^{-1} \int_{X_0}^{X_0+\lambda} \frac{\partial Y_L}{\partial X} p|_{Y_L} dX, \tag{2.8a}$$

$$F_{Y,L} = F_{Yv,L} + F_{Yp,L} = \lambda^{-1} \int_{X_0}^{X_0+\lambda} \left[\frac{\partial Y_L}{\partial X} \left(Re \frac{du_0}{dY} + \frac{\partial u_1}{\partial Y} + \frac{\partial v_1}{\partial X} \right) \bigg|_{y_L} - 2 \frac{\partial v_1}{\partial Y} \bigg|_{Y_L} \right] dX$$

$$+ \lambda^{-1} \int_{X_0}^{X_0+\lambda} p|_{Y_L} dX, \tag{2.8b}$$

where X_0 is a convenient reference point, $F_{Xp,L}$ and $F_{Yp,L}$ denote the pressure contributions, while $F_{Xv,L}$ and $F_{Yv,L}$ stand for the viscous contributions. The X-pressure force $F_{Xp,L1}$ created by the periodic pressure component is defined separately, i.e.

$$F_{Xp,L1} = -\lambda^{-1} \int_{X_0}^{X_0+\lambda} \frac{\partial Y_L}{\partial X} p_1|_{Y_L} dX, \tag{2.8c}$$

as it is of interest in the discussion of flow mechanics. A similar process applied to the upper wall yields

$$\sigma_{X,U} = \sigma_{Xv,U} = \left(Re \frac{du_0}{dY} + \frac{\partial u_1}{\partial Y} \right) \bigg|_{Y=1}, \tag{2.9a}$$

$$\sigma_{Y,U} = \sigma_{Yv,U} + \sigma_{Yp,U} = 2 \frac{\partial v_1}{\partial Y} \bigg|_{Y=1} - p|_{Y=1}, \tag{2.9b}$$

where $(\sigma_{Xv,U}, \sigma_{Yv,U})$ and $\sigma_{Yp,U}$ denote the viscous and pressure contributions, respectively. The X- and Y-components of the total force $(F_{X,U}, F_{Y,U})$ can be determined as

$$F_{X,U} = F_{Xv,U} = \lambda^{-1} \int_{X_0}^{X_0+\lambda} \left[\left(Re \frac{du_0}{dY} + \frac{\partial u_1}{\partial Y} \right) \bigg|_{Y=1} \right] dX, \tag{2.10a}$$

$$F_{Y,U} = F_{Yv,U} + F_{Yp,U} = 2\lambda^{-1} \int_{X_0}^{X_0+\lambda} \frac{\partial v_1}{\partial Y} \bigg|_{Y=1} dX - \lambda^{-1} \int_{X_0}^{X_0+\lambda} p|_{Y=1} dX, \tag{2.10b}$$

where $F_{Yp,U}$ denotes the pressure contributions, while $F_{Xv,U}$ and $F_{Yv,U}$ stand for the viscous contributions.

The vibration-induced change of surface forces is of primary interest. They are expressed as

$$\Delta F_{Xv,U} = F_{Xv,U} + 2Re, \quad \Delta F_{Xv,L} = F_{Xv,L} + 2Re, \quad \Delta F_{Xp,L1} = F_{Xp,L1}. \tag{2.11a}$$

The final force of interest is the force created by the mean pressure gradient $F_{Xp,m} = \partial p/\partial X|_{mean}$ per unit length and unit width of the channel. Its change due to vibrations is defined as

$$\Delta F_{Xpm} = 2 \left(\frac{\partial p}{\partial X} \bigg|_{mean} - Re^2 \frac{dp_0}{dX} \right) = -2B_{mod}. \tag{2.11b}$$

3. Solution method

The analysis is simplified by introducing a frame of reference moving with the wave phase speed using Galileo's transformation of the form

$$y = Y, \quad x = X - ct. \tag{3.1}$$

Its use leads to a steady problem with the form

$$(Re\,u_0 + u_1 - c)\frac{\partial u_1}{\partial x} + Re\,v_1\frac{\partial u_0}{\partial y} + v_1\frac{\partial u_1}{\partial y} = B_{mod} - \frac{\partial p_1}{\partial x} + \frac{\partial^2 u_1}{\partial x^2} + \frac{\partial^2 u_1}{\partial y^2}, \tag{3.2a}$$

$$(Re\,u_0 + u_1 - c)\frac{\partial v_1}{\partial x} + v_1\frac{\partial v_1}{\partial y} = -\frac{\partial p_1}{\partial y} + \frac{\partial^2 v_1}{\partial x^2} + \frac{\partial^2 v_1}{\partial y^2}, \tag{3.2b}$$

$$\frac{\partial u_1}{\partial x} + \frac{\partial v_1}{\partial y} = 0, \tag{3.2c}$$

$$y = 1: \quad u_1 = 0, \quad v_1 = 0, \tag{3.2d}$$

$$y = y_L(x): \quad u_1 = -Re\,u_0, \quad v_1 = \tfrac{1}{2}\,c\alpha A \sin(\alpha x), \tag{3.2e}$$

$$Q = \left\{\int_{y_L(x)}^{1} [Re\,u_0(y) + u_1(x, y)]\,\mathrm{d}y\right\}\bigg|_{mean} = \frac{4}{3}Re, \tag{3.2f}$$

where locations of the boundaries are given as

$$y_U(x) = 1, \quad y_L(x) = -1 + \tfrac{1}{2}A\cos(\alpha x). \tag{3.2g,h}$$

In the above, subscript 'mean' refers to averaging over one wavelength.

We shall now look at waves with arbitrary wavelengths, and their analysis requires numerical methods. As the first step, we eliminate pressure using stream function modifications ψ_1, i.e. $u_1 = \partial\psi_1/\partial y$, $v_1 = -\partial\psi_1/\partial x$, arriving at the flow problem of the form

$$-\nabla^2(\nabla^2\psi_1) + (Re\,u_0 - c)\frac{\partial}{\partial x}\nabla^2\psi_1 - Re\frac{\mathrm{d}^2 u_0}{\mathrm{d}y^2}\frac{\partial\psi_1}{\partial x} = -\left(\frac{\partial\psi_1}{\partial y}\frac{\partial}{\partial x} - \frac{\partial\psi_1}{\partial x}\frac{\partial}{\partial y}\right)\nabla^2\psi_1, \tag{3.3a}$$

$$y = 1: \quad \frac{\partial\psi_1}{\partial y} = 0, \quad \frac{\partial\psi_1}{\partial x} = 0, \tag{3.3b,c}$$

$$y = y_L(x): \quad \frac{\partial\psi_1}{\partial y} = -Re\,u_0, \quad \frac{\partial\psi_1}{\partial x} = -\frac{1}{2}\,c\alpha A \sin(\alpha x), \tag{3.3d,e}$$

$$Q = [(Re\,\psi_0 + \psi_1)|_{y=1} - (Re\,\psi_0 + \psi_1)|_{y=y_L(x)}]|_{mean} = \frac{4}{3}Re. \tag{3.3f}$$

Condition (3.3e) can be written in a different form by noting that variations of the stream function of the complete flow $\psi_T = Re\,\psi_0 + \psi_1$ along the lower wall can be written as

$$\mathrm{d}\psi_{T,L} = \left(\frac{\partial\psi_T}{\partial x}\,\mathrm{d}x + \frac{\partial\psi_T}{\partial y}\,\mathrm{d}y\right)\bigg|_{y_L(x)} = -\frac{1}{2}\,c\alpha A \sin(\alpha x). \tag{3.4}$$

Integration along this wall results in

$$\psi_{T,L}(x) = c[y_L(x) - y_L(x_0)], \tag{3.5}$$

where the constant of integration was set by assuming that $\psi_{T,L}(x_0) = 0$ with x_0 representing an arbitrary point at this wall. At the upper wall,

$$\psi_{T,U}(x) = g, \tag{3.6}$$

where g denotes a constant that needs to be determined from the flow rate constraint. Since $Q = \psi_{T,U} - \psi_{T,L}$ and its mean value is determined by (3.3f), the final form of (3.6) can be expressed as

$$g = -c\; y_L(x_0) - c + \frac{4}{3}Re. \tag{3.7}$$

Boundary conditions (3.3c) and (3.3e) combined with the flow rate constraint (2.4f) can now be written as

$$y = 1: \quad \psi_1 = -c[1 + y_L(x_0)], \tag{3.8a}$$

$$y = y_L(x): \quad \psi_1 = c[1 - y_L(x_0)] - Re\,\psi_0. \tag{3.8b}$$

The Chebyshev and Fourier expansions are used to provide a spectrally accurate discretization of the field equations. Since waves are periodic, all unknowns can be expressed as Fourier expansions of the form

$$q_1(x, \hat{y}) = \sum_{m=-N_M}^{m=+N_M} q_1^{(m)}(\hat{y})\, e^{im\alpha x}, \tag{3.9}$$

where q_1 stands for any of the following quantities: $\psi_1,\ v_1,\ u_1, p_1,\ \widehat{v_1 v_1},\ \widehat{u_1 u_1},\ \widehat{u_1 v_1}$, the modal functions $q_1^{(m)}$ satisfy the reality conditions, i.e. $q_1^{(m)}$ are the complex conjugates of $q_1^{(-m)}$, respectively. The modal functions $q_1^{(m)}(\hat{y})$ were expressed as Chebyshev expansions. The linear algebraic equations for the Chebyshev expansion coefficients were constructed using the Galerkin projection method. Spectral methods are not suitable for handling irregular geometries; this difficulty was overcome by implementing the immersed boundaries concept (IBC). Here we follow the process described by Szumbarski & Floryan (1999), Husain & Floryan (2008a,b, 2010) and Husain, Szumbarski & Floryan (2009). The boundary conditions were replaced by constraints imposed using the tau concept (Canuto *et al.* 1992). The condition for determination of the unknown pressure gradient correction B_{mod} is formed by substituting Fourier expansions for all unknowns into the *x*-momentum equation and extracting mode zero.

The overall algorithm is gridless and very flexible when a change of wave shape is of interest – the algorithm can be adapted to analyses of multiple geometries with minimal user involvement. Computations were carried out with a minimum of five digits accuracy – this dictated selection of the number of Fourier modes and the number of Chebyshev polynomials. The algorithm provides access to machine accuracy if required.

We have limited the following discussion to waves with amplitudes $A < 0.05$ – although subjective, this limit is dictated by our interests in the potential use of piezoelectric actuators for creating such waves. In the next section, we begin a discussion with a summary of the peristaltic effect and focus on vibration acting along one wall only.

4. Peristaltic pumping

We eliminate flow ($Re = 0$). Vibrations produce a distributed propulsive force which pumps fluid in the wave direction with the flow rate Q dependence on the wavenumber and phase speed illustrated in figure 2(*a*). Flow rate remains nearly independent of α for long
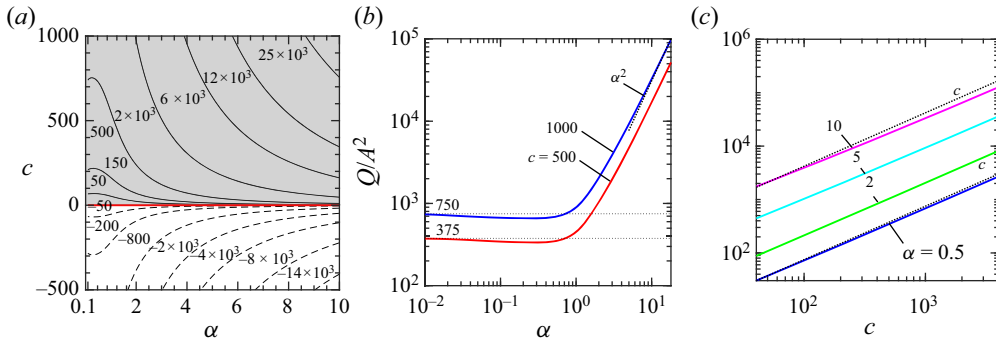
Figure 2. Variations of the flow rate Q/A^2 as a function of α and c. In panel (*a*), solid and dashed lines represent the positive and negative Q, the red line represents conditions resulting in $Q = 0$ and the grey colour identifies the state when Q is positive. Horizontal cuts through the plot displayed in panel (*a*) for $c = 500, \ 1000$ are shown in panel (*b*), and vertical cuts for $\alpha = 0.5, \ 2, \ 5, \ 10$ are shown in panel (*c*).

waves and increases proportionally to α^2 for short waves (figure 2*b*). It increases nearly proportionally to c in the range of c considered in this analysis (figure 2*c*). The structure of solution for fast waves is given analytically by Floryan, Haq & Bassom (2023*b*). In the next section, we focus on the pressure gradient-driven flow and investigate modifications caused by simple sinusoidal vibrations.

5. Vibration-induced velocity field modifications

We consider the same vibrations as in § 4. Instantaneous vector lines of velocity modifications $\boldsymbol{u}_1 = \boldsymbol{u} - Re\,\boldsymbol{u}_0$ illustrate the topology of the velocity field. The results displayed in figure 3 for the small ($\alpha = 0.1$), medium ($\alpha = 1.5$) and large ($\alpha = 10$) wavenumbers suggest that variations in Re marginally change flow topologies. Long wavelength vibrations (figure 3*a*,*d*,*g*,*j*) produce modification with a sloshing pattern where the forward movement occurs around the wave troughs and the backward movement near the crests. The analytic description of the velocity field (see Appendix A for details) has the form

$$u = \frac{Re}{1 - \frac{1}{4}A\cos(\alpha x)}(1 - \eta^2) - c\frac{3A\,\cos(\alpha x)}{8\left[1 - \frac{1}{4}A\cos(\alpha x)\right]}(1 - \eta^2) + 0(\alpha), \quad \tilde{v}_0 = 0(\alpha),$$

(5.1)

where $\eta = (y - 1)[1 - \frac{1}{4}A\cos(\alpha x)]^{-1} + 1$. The first term on the right-hand side represents the (passive) 'groove effect', i.e. flow modulations produced by stationary grooves, and the second term describes the 'wave effect', which periodically changes direction, creating sloshing. Reynolds number plays a role in setting up the 'groove effect', while the sloshing effect is Re-independent. The short wavelength vibrations (figure 3*c*,*f*,*i*,*l*) produce a boundary layer near the vibrating wall and an unmodulated uniform flow above it. We shall refer to this flow pattern as the moving-wall regime, with a detailed explanation of the origin of this term given later in this discussion. Flow topologies at intermediate values of α (figure 3*b*,*e*,*h*,*k*) represent a hybrid between the sloshing and the moving-wall structures.

Profiles of u_1 provide additional information about the structure of the velocity field. The long wavelength vibrations create modifications of appreciable size over the entire
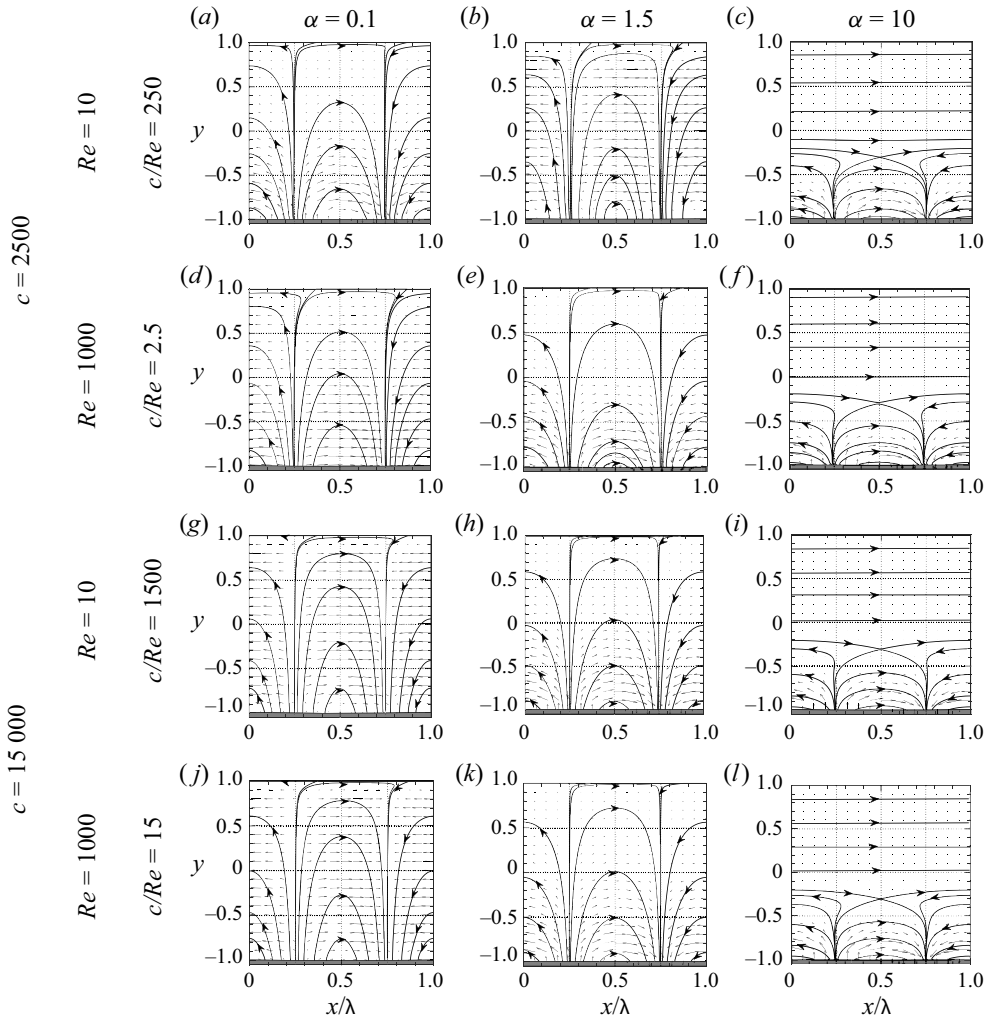
Figure 3. Topologies of the vibration-modified flow field (u_1) for groove amplitude $A = 0.0025$.

width of the channel. The resulting periodic changes of direction lead to the sloshing effect (see figure 4*a,d,g,j*). The short-wave vibrations create modifications consisting of a boundary layer near the vibrating wall containing the intense streamwise modulations and an unmodulated stream above this boundary layer. The resulting flow pattern is referred to as the moving-wall pattern (see figure 4 *c,f,i,l*). In the in-between zone, the flow morphs continuously from the small-α to the large-α forms. These states are illustrated in figure 4(*b,e,h,k*). Overall, velocity distributions change marginally with *Re*, and their profiles are hardly affected by changes in *c*. Their magnitudes are, however, roughly proportional to *c*. It is interesting to note that flow modifications have a generic form regardless of the purpose of vibrations, being pumping (Floryan *et al.* 2021), propulsion (Haq & Floryan 2022) or resistance reduction (Floryan & Haq 2022).

The flow modifications induced by short waves demonstrate the mechanism of reduction of pressure losses. Vibrations tend to pump the fluid to the right within the boundary layer, with the edge of the boundary layer acting as a wall moving to the right with
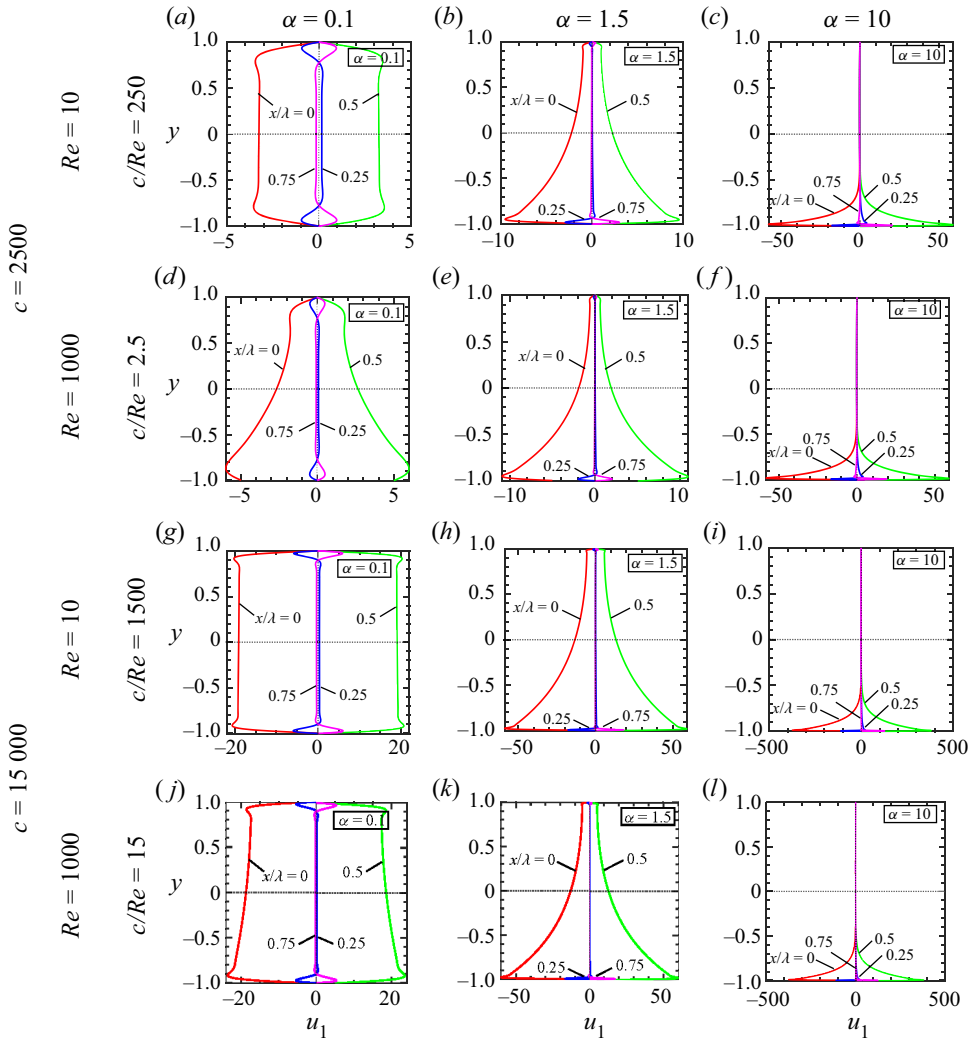
Figure 4. The distributions of the *u*-velocity modification (u_1) at $x/\lambda = 0$, 0.25, 0.5, 0.75 for groove amplitude $A = 0.0025$.

an apparent velocity U_{ap}. Since the flow rate cannot be affected by vibrations, the flow system generates a positive pressure gradient producing flow to the left. The velocity modification u_1 is *x*-independent outside the boundary layer and, thus, must have a form of Couette–Poiseuille flow with zero flow rate. The edge of the boundary layer acts as a wall moving to the right (Couette part) and the pressure gradient correction is responsible for the Poiseuille component directed to the left. Parabola with coefficients determined by imposing the no-slip condition at the upper plate and the flow rate constraint, i.e.

$$u_1(y = 1) = 0, \quad \int_{-1}^{1} u_1 \, \mathrm{d}y = 0, \qquad (5.2a,b)$$

approximates the velocity field outside the boundary layer. The third condition involves either the use of pressure gradient correction (B_{mod}) determined numerically, and this
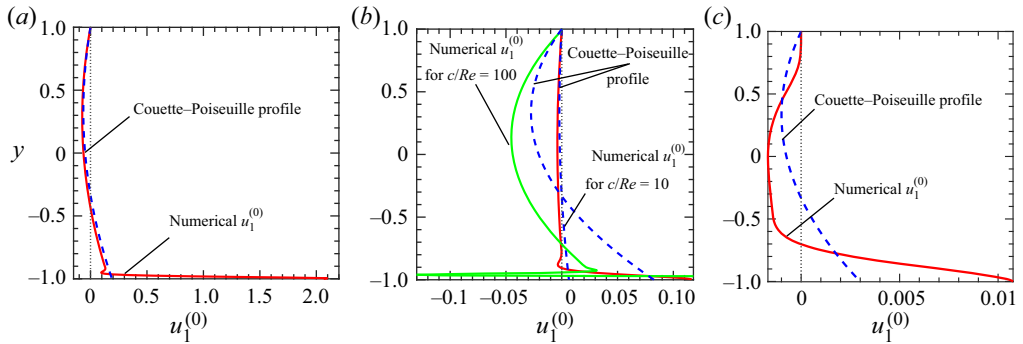
968 A8-11

Figure 5. Distributions of $u_1^{(0)}$ for (a) $\alpha = 10$, (b) $\alpha = 1.5$ and (c) $\alpha = 0.1$. All results are for $Re = 100$, $c/Re = 10$, $A = 0.005$. The blue dashed line indicates the Couette–Poiseuille velocity profile. The green line in panel (b) is for $c/Re = 100$ with other conditions remaining unchanged.

leads to the velocity distribution of the form

$$u_1(y) = \frac{-B_{mod}}{6}(3y^2 - 2y - 1), \tag{5.3}$$

or matching the analytic u_1 with the numerical u_1 at a point well outside the boundary layer. Results displayed in figure 5 demonstrate an excellent agreement between the numerically determined u_1 and the fitted Couette–Poiseuille flow. The same argument applies to any α as the flow system must generate an x-independent backward flow component to maintain the prescribed flow rate, and this component requires a proper pressure gradient. The matching of the complete flow with the Couette–Poiseuille flow is perfect for $\alpha = 10$ (figure 5a) and it is reasonably good for $\alpha = 1.5$ (figure 5b). The total flow remains qualitatively similar to the Couette–Poiseuille flow even for $\alpha = 0.1$ (figure 5c) – this is surprising as the spatial modulations extend across the whole channel for small α so the mode zero of u_1 is not expected to be well approximated by the Couette–Poiseuille flow.

The apparent wall velocity U_{ap} is determined by extending (5.3) to the lower wall. Results displayed in figure 6 demonstrate that U_{ap} is proportional to A^2, it increases proportionally to α^2 for large enough α, and is proportional to c for large c values. The concept of apparent wall velocity works reasonably well even for very small α where the boundary layer does not exist, as illustrated in figure 5(c).

Data displayed in figures 4(b,e,h,k) and 5(b) demonstrate that an increase of c does not eliminate sloshing – the amplitude of sloshing increases with c while the amplitude of $u_1^{(0)}$ increases implying a more significant pressure gradient correction.

The last question we wish to address in this section is to explain how the effects of wall actuation are transferred into the flow interior. This question is addressed using the small ($A \to 0$) wave amplitude solution – details of this solution are presented in Appendix B. It suffices to state that waves produce periodic modulations at level $0(A)$, which combine at level $0(A^2)$ producing an aperiodic component that determines the pressure gradient correction. The following system describes the $0(A^2)$ aperiodic part of flow modifications:

$$D^2\tilde{u}_2^{(0)} - B_2 = \tilde{v}_1^{(1)}D\tilde{u}_1^{(-1)} + \tilde{v}_1^{(-1)}D\tilde{u}_1^{(1)}, \tag{5.4a}$$

$$\tilde{u}_2^{(0)}(1) = 0, \quad \tilde{u}_2^{(0)}(-1) = -\tfrac{1}{4}(D\tilde{u}_1^{(1)} + D\tilde{u}_1^{(-1)}) - \tfrac{1}{8}Re, \quad \psi_2^{(0)}(1) - \psi_2^{(0)}(-1) = -\tfrac{1}{8}Re, \tag{5.4b}$$
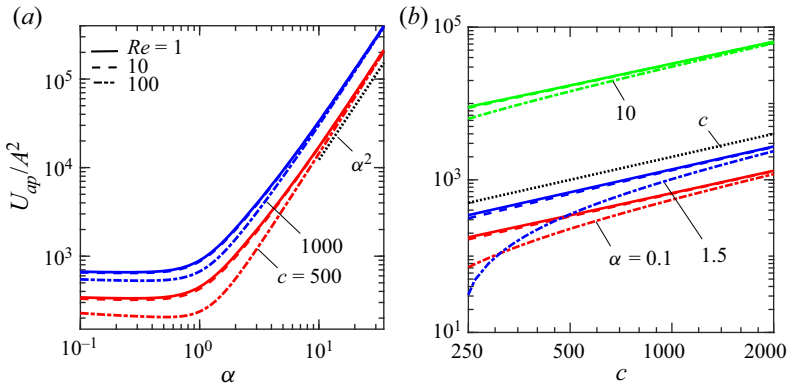
Figure 6. Variation of the apparent lower wall velocity U_{ap}/A^2 (*a*) as a function of α for $c = 500$, 1000 and (*b*) as a function of c for $\alpha = 0.1$, 1.5, 10.

where B_2 stands for the pressure gradient correction. Notation is explained in Appendix B. This solution shows that there are two mechanisms associated with momentum transfer. The first one, which is indirect, involves vibrations creating flow field modification which combine to form Reynolds stresses (right-hand side of (5.4*a*)). The second mechanism involves a direct momentum transfer as the second boundary condition in (5.4*b*) acts as a slip condition creating movement in the vicinity of the wall.

6. Pressure losses

Flow through a conduit is driven by a pressure gradient whose magnitude is dictated by the need to overcome the friction between the fluid and the bounding walls. As discussed in the previous section, the required pressure gradient can be reduced because vibrations provide a part of the driving force through the peristaltic effect. Modifications of the velocity field change the wall shear stresses, so a detailed flow field analysis is required to quantify pressure losses. The flow system is characterized by natural frequencies which could be excited by vibrations – the potential resonance may interfere with the peristaltic effect and affect the wall shear. The natural frequencies are characterized by the complex amplification rate $C = C_r + iC_i$ which is dictated by a solution of the Orr–Sommerfeld equation discussed in Appendix C. Here, C_r denotes the phase speed and C_i stands for the amplification rate. The natural frequencies are attenuated for $Re < 5772.22$ (Orszag 1971) with the attenuation rate increasing with a reduction of Re. This process is illustrated in figure 9 for the least attenuated wave with $\delta = 1$, where δ stands for the wavenumber of natural waves (see Appendix C); it is obvious that one must take $\alpha = \delta$ to compare both types of waves. The attenuation rapidly increases for $Re < 100$, which suggests that the near resonance effects are negligible. The smallest Re leading to the actual resonance is $Re = 5772.22$, which occurs only for vibration waves with $\alpha = 1.02$ and $c/Re = 0.2639$ (Orszag 1971), and it produces flow modifications symmetric around the channel centreline. Vibration-induced flow modifications are non-symmetric as only one wall vibrates, so the difference in symmetries must affect the outcome of the resonance. The range of waves capable of activating resonance increases as Re increases above 5772.22, while waves outside this range are in near resonance. The following discussion is divided into the small-Re flows ($Re < 100$) where the resonance effects are negligible, the intermediate-Re flows ($100 < Re < 5000$) where the near resonance effects are expected to play a role and the large-Re flows ($Re \geq 5000$) where the actual resonance may occur.

6.1. *Small-Re flows (Re ≤ 100)*

We begin our discussion with the low-*Re* flows where resonance is negligible. The pressure gradient correction *B* for the long wavelength vibrations can be determined analytically (see Appendix A for details), i.e.

$$B_{mod} = Re^2 \frac{\mathrm{d}p_0}{\mathrm{d}x} - \frac{\mathrm{d}\tilde{p}_{-1}}{\mathrm{d}\xi}\bigg|_{mean} = 2Re\left[-1 + \left(1 + \frac{A^2}{32}\right)\left(1 - \frac{A^2}{16}\right)^{-5/2}\right] - \frac{9}{32}cA^2\left(1 - \frac{A^2}{16}\right)^{-5/2}.$$
(6.1)

The first term on the right-hand side represents the (passive) 'groove effect' and is always positive, i.e. grooves always increase pressure losses. The second term on the right-hand side describes the 'wave effect', which is negative for the downstream propagating waves ($c > 0$) and favourable for the upstream propagating waves ($c < 0$). Reynolds number plays a role in setting up the 'groove effect', which is proportional to *Re*, while the 'wave effect' is *Re*-independent but proportional to *c*. The overall reduction of pressure losses is achieved using sufficiently fast waves propagating in the downstream direction so that the 'wave effect' overcomes the 'groove effect'. The wave speed c_1 required to bring the pressure gradient correction to zero is

$$c_1 = \frac{64Re}{9A^2}\left[1 + \frac{A^2}{32} - \left(1 - \frac{A^2}{16}\right)^{5/2}\right],$$
(6.2)

and the wave speed c_2 required to bring the overall pressure gradient to zero is

$$c_2 = \frac{64Re}{9A^2}\left(1 + \frac{A^2}{32}\right).$$
(6.3)

The above results demonstrate that increasing wave amplitude reduces the required wave speed. Waves faster than c_2 require using an opposite pressure gradient to prevent the fluid from accelerating. Faster flows require faster waves to reduce pressure losses, as both c_1 and c_2 increase with *Re*.

Variations of the normalized pressure gradient $B_{norm} = B_{mod}/2Re\,A^2$ are illustrated in figure 8. The factor $2Re$ represents the pressure gradient of the reference flow, so the ratio $B_{mod}/2Re$ expresses pressure gradient correction as a fraction of the reference pressure gradient. The factor A^2 is added to account for variations in the wave amplitude as B_{mod} is proportional to A^2 for small amplitudes being of interest in this analysis. The right axes display *c* in absolute scale defined in §2. The left axes show c/Re – since the maximum velocity of the reference flow is *Re*, the ratio c/Re measures the wave speed in terms of the maximum reference velocity. We shall refer to waves with speeds larger than *Re* as supercritical waves, while the slower waves will be referred to as subcritical. Velocity modifications created by subcritical waves are characterized by critical layers where the wave speed equals flow velocity.

The distinction between the supercritical and subcritical waves is irrelevant for small *Re*. Results for $Re = 1$ demonstrate that nearly all downstream propagating waves reduce pressure losses (see figure 8a). In contrast, the upstream propagating waves increase pressure losses. The results shown in figure 8(*b*) demonstrate that an increase of *Re* requires faster waves to reduce pressure losses, and the minimum required wave speed depends on the wavenumber. Use of waves with $c/Re > 2.3$ guarantees a reduction of pressure losses regardless of the wavenumber. In this zone, the magnitude of reduction increases with *c* and α in a regular manner showing that fast, short-wavelength waves
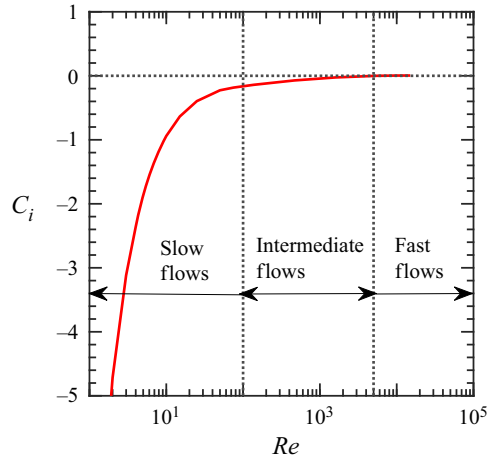
968 A8-14

Figure 7. Variations of the attenuation rate of the least attenuated natural flow frequency for $\delta = \alpha = 1$.
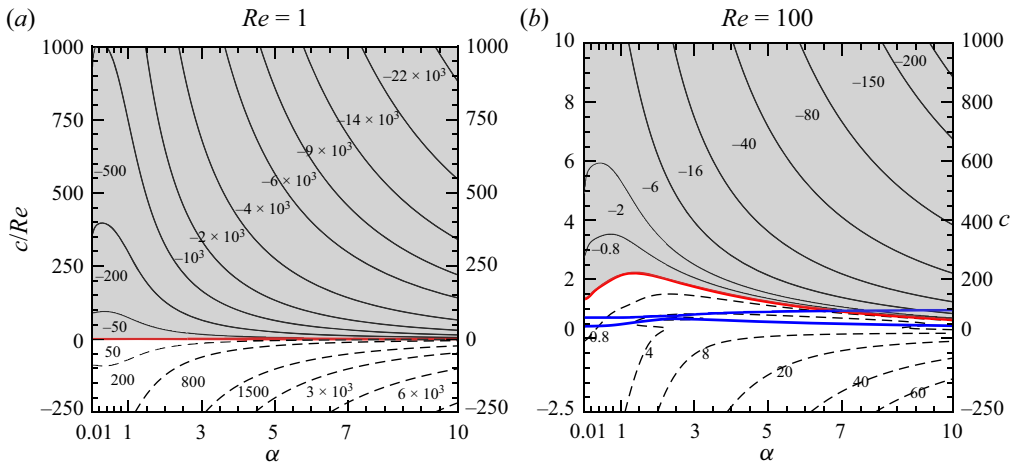

Figure 8. Variations of the pressure gradient correction $B_{norm} = B_{mod}/2\,Re\,A^2$ as a function of α and c for $Re = 1, 100$ (panels *a,b*, respectively). Solid and dashed lines represent the negative and positive values, respectively. Grey colour identifies conditions resulting in a reduction of pressure losses. The red line identifies conditions that do not affect pressure losses. Zones between the blue lines represent the range of natural flow frequencies.

are most effective in reducing losses. The zone with $1 < c/Re < 2.3$ can be viewed as a transition zone where processes dominating flow response to subcritical waves are replaced by processes associated with supercritical waves. This distinction becomes more prominent for larger Re, as is shown later in this presentation.

We can gain insight into the flow response by investigating variations of B_{mod} along specific cuts through the parameter space. Figure 9(*a*) shows that the pressure gradient correction is nearly independent of α for long waves but begins to increase proportionally to α^2 for $\alpha > 1$. It is possible to reduce pressure losses down to zero if short enough waves are used, and an opposite pressure gradient may have to be used to prevent flow acceleration. Dependence of B_{mod} on c is complex for slow waves but shows an increase proportional to c for fast enough waves (see figure 9*b*). The minimum c required for the
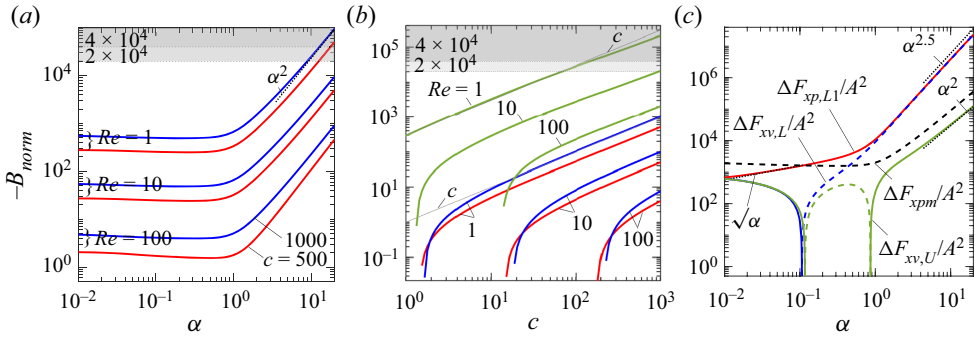
968 A8-15

Figure 9. Variations of the pressure gradient correction $B_{norm} = B_{mod}/2\,Re\,A^2$ (*a*) as a function of α and (*b*) as a function of c ($\alpha = 0.5$, red line; $\alpha = 1.5$, blue line; $\alpha = 30$, green line). The dark grey colour identifies conditions requiring the opposite pressure gradient to slow the fluid. The light grey colour identifies conditions leading to a minimum of 50% pressure gradient reduction. (*c*) Variations of the modifications of the x-components of forces $\Delta F_{xv,L}/A^2$ (blue line), $\Delta F_{xv,U}/A^2$ (green line) and $\Delta F_{xp,L1}/A^2$ (red line) as functions of α for $Re = 100$, $c = 1000(c/Re = 10)$. The solid (dashed) lines correspond to positive (negative) values. The black dashed line illustrates the additional x-pressure force $\Delta F_{xpm}/A^2 = -2B_{mod}/A^2$ generated by the pressure gradient correction.

initiation of the regular, c-proportional growth of B_{mod} varies widely with α and Re. It is possible to eliminate pressure losses if fast enough waves are used. Analysis of results displayed in figure 9(*a*,*b*) shows that the effectiveness of a specific wave decreases with an increase of Re, i.e. the pressure gradient correction represents a smaller fraction of the reference pressure gradient. This reduction happens because the wave penetration into the flow decreases as Re increases. The reduction can be compensated through an increase in wave velocity.

Analysis of an interplay of different forces acting on the fluid provides further insight into the flow response. Here we select the upper end of figure 8(*b*) where B_{mod} varies with c and α in a very regular manner. Figure 9(*c*) illustrates typical variations of $\Delta F_{xv,L}$, $\Delta F_{xv,U}$ and $\Delta F_{xp,L1}$ (see (2.11) for definitions) as functions of α for c. The surface pressure force $F_{xp,L1}(= \Delta F_{xp,L1})$ at the vibrating wall reaches a constant in the limit $\alpha \to 0$. There is a range of α ending at $\alpha \approx 0.5$ where this force increases proportionally to $\alpha^{1/2}$ and this rate increases to $\alpha^{2.5}$ when $\alpha > 1$. Vibration-induced change of viscous force at the lower wall $\Delta F_{xv,L}$ assists with the fluid movement for $\alpha < 0.1$ but opposes this movement for larger α. Change of the viscous force at the upper wall $\Delta F_{xv,U}$ assists fluid movement for $\alpha < 0.1$ and $\alpha > 0.9$ but opposes this movement for α in between these limits. Changes in the viscous and pressure forces at the vibrating wall are dominant for $\alpha > 1$ – they oppose each other with their magnitudes increasing proportionally to $\alpha^{2.5}$. The increase in the magnitude of $\Delta F_{xp,L1}$ exceeds that of $\Delta F_{xv,L}$ resulting in a reduction of the required pressure gradient force $F_{xp,m}$ – this reduction is proportional to α^2. Change of the viscous force at the upper wall $\Delta F_{xv,U}$ also increases proportionally to α^2 but it plays a marginal role due to its relatively small magnitude.

To determine the energy cost of vibrations, we take a scalar product of the momentum equation with a velocity vector and integrate it over a control volume consisting of a channel section extending over one wavelength $\lambda = 2\pi/\alpha$ in the x-direction. The resulting

expression has the form

$$\iint \left[u^2 \frac{\partial u}{\partial x} + uv \frac{\partial u}{\partial y} + uv \frac{\partial v}{\partial x} + v^2 \frac{\partial v}{\partial y} - c \left(u \frac{\partial u}{\partial x} + v \frac{\partial v}{\partial x} \right) \right] dS$$

$$= -\iint \left(u \frac{\partial p}{\partial x} + v \frac{\partial p}{\partial y} \right) dS + \iint \left(u \frac{\partial^2 u}{\partial x^2} + u \frac{\partial^2 u}{\partial y^2} + v \frac{\partial^2 v}{\partial x^2} + v \frac{\partial^2 v}{\partial y^2} \right) dS, \quad (6.4)$$

where the integration domain S is defined as $y \in [y_L(x), 1]$, $x \in [0, \lambda]$. Integration by parts and use of the x-periodicity property and continuity equation lead to

$$P_{mpg} = P_\varepsilon + P_{wv} - P_{wp} , \quad (6.5a)$$

where

$$P_{mpg} = (2Re + B_{mod}) \, Q \quad (6.5b)$$

describes the power supplied by the mean pressure gradient. The three terms on the right-hand side of (6.5a) are defined by

$$P_\varepsilon = \lambda^{-1} \iint \left[\left(\frac{\partial u}{\partial x} \right)^2 + \left(\frac{\partial u}{\partial y} \right)^2 + \left(\frac{\partial v}{\partial x} \right)^2 + \left(\frac{\partial v}{\partial y} \right)^2 \right] dS, \quad (6.6a)$$

$$P_{wv} = \lambda^{-1} \int_0^\lambda \left(v \frac{\partial v}{\partial x} \frac{dy_L}{dx} - v \frac{dv}{dy} \right)_{y=y_L(x)} dx, \quad P_{wp1} = \lambda^{-1} \int_0^\lambda (vp_1)_{y=y_L(x)} \, dx, \quad (6.6b,c)$$

with P_ε standing for the rate of dissipation of energy, P_{wv} denoting the rate of work done by viscous forces at the vibrating wall and P_{wp1} standing for the work rate done by the periodic pressure component at the vibrating wall.

The external power is required to overcome dissipation and viscous work at the lower wall – this power can be reduced by pressure work at the lower wall. Changes produced by vibrations are defined as

$$\Delta P_{mpg} = P_{mpg} - P_{mpg,0} = B_{mod} Q, \quad \Delta P_\varepsilon = P_\varepsilon - P_{\varepsilon,0}, \quad (6.7a,b)$$

$$\Delta P_{wv} = P_{wv} - P_{wv,o} = P_{wv}, \quad \Delta P_{wp1} = P_{wp1} - P_{wp,0} = P_{wp1}, \quad (6.7c,d)$$

and are of the main interest. In the above, quantities with subscript 0 refer to the reference flow (smooth channel) and are

$$P_{mpg,0} = 2Re \, Q, \quad P_{\varepsilon,0} = \tfrac{8}{3} Re^2, \quad P_{wv,o} = 0, \quad P_{wp,0} = 0. \quad (6.8a\text{–}d)$$

Results displayed in figure 10 show that viscous work at the lower wall is generally negligible, and the system response involves interplay between the mean-pressure-gradient power, the pressure work at the lower wall and the dissipation. There are two distinct energy fluxes in the (c, α)-plane. The first zone is characterized by a monotonic increase in the magnitude of energy fluxes with an increase of c and α. This zone generally overlaps with the supercritical waves. The dominant fluxes are the wall pressure work – most of it is used for increasing dissipation, and leftovers are used to reduce pressure losses. A reduction of pressure losses characterizes this zone. The second zone overlaps with subcritical waves. Here variations of energy fluxes with c and α are somewhat irregular, with the wall pressure work becoming negative, which means that fluid does the work. The pressure losses increase as they provide the energy required to overcome wall pressure work, with dissipation playing a minor role in the energy balance. This effect is not visible
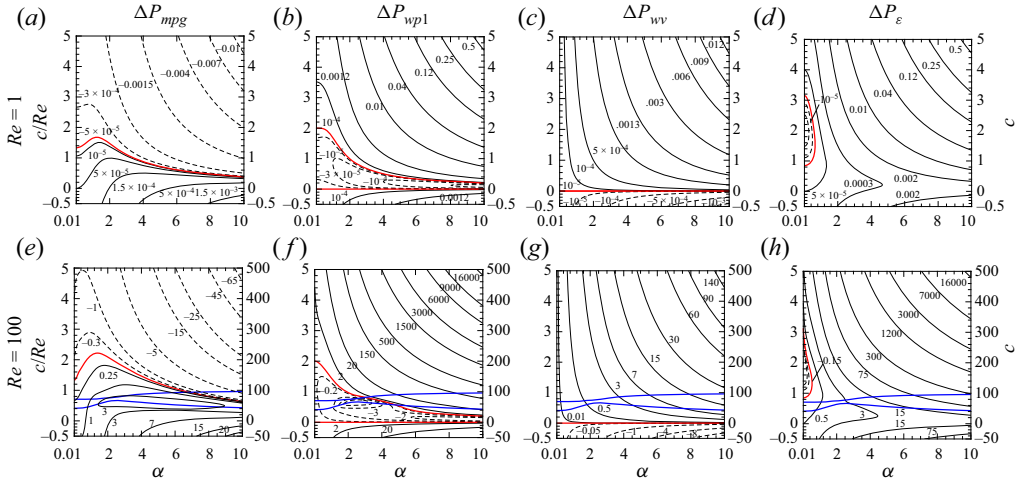
Figure 10. Variations (a,e) of change in power supplied by the mean pressure gradient ΔP_{mpg}, (b,f) of the rate work done by pressure at the lower wall $P_{wp1}(= \Delta P_{wp1})$, ($c,g$) of the rate of work done by the viscous forces at the lower wall $P_{wv}(= \Delta P_{wv})$ and (d,h) of the increase in the dissipation ΔP_ε as functions of α and c/Re. All results are for $A = 0.005$. Panels (a–d) display data for $Re = 1$ and panels (e–h) for $Re = 100$. The solid (dashed) lines represent positive (negative) values. The red colour identifies zero isolines. Zones between the blue lines represent the range of natural frequencies of the OS modes.

for $Re = 1$ (see figure 10a–d) but can be identified for $Re = 100$ (see figure 10e–h) – its strength increases with Re as discussed later. The border between these two zones is not well demarcated as the transition between both types of responses is gradual – this transition occurs for $1 < c/Re < 2$.

6.2. *Intermediate-Re flows* ($100 < Re < 5000$)

An increase in flow velocity allows for a near resonance between a particular class of vibrations and the natural flow frequencies. The natural frequencies are determined by adding small perturbations of the form

$$[u_1, v_1, p_1](X, Y, t) = [\hat{u}_1, \hat{v}_1, \hat{p}_1] e^{i\delta(X-Ct)} + CC \qquad (6.9)$$

to the reference flow and solving the relevant equations. In (6.9), CC stands for the complex conjugate, $C = C_r + iC_i$ with C_r being the phase speed and C_i being the amplification rate. Here, $C_i \leq 0$ identifies conditions when either resonance or near resonance may occur, while $C_i > 0$ provides a measure of the 'distance' from the resonance where complex responses are expected (such perturbations draw energy from the flow without involving vibrations). Determination of C is explained in Appendix C. Creation of a resonance requires the use of vibrations matching the natural flow frequencies, i.e. vibrations with the wavenumber $\alpha = \delta$ and the phase speed $c = C_r$. Variations of C_r and C_i as functions of α and Re illustrated in figure 11 demonstrate that resonance is possible only for a limited range of α and c which change with Re, i.e. the resonance may occur for $\alpha \in (\sim 0.8, \sim 1.1)$ and $c \in (\sim 0.2, \sim 0.3)$ when $Re \geq 5772.22$. The use of vibrations either with large α or with large c eliminates resonance.

Since a near resonance is possible in flows with $100 < Re < 5000$, it is interesting to determine how it can affect pressure losses. Variations of B_{mod} as a function of α and c illustrated in figure 12 demonstrate that the border between the reduction and increase
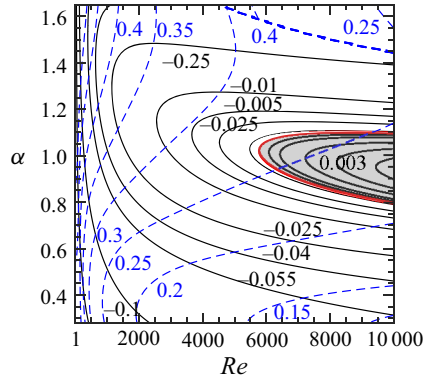
Figure 11. Natural frequencies and the corresponding wavenumbers for the plane Poiseuille flow. The solid black lines indicate the amplification rate (C_i) of the TS waves with the solid red line marking the neutral conditions ($C_i = 0$), the blue dashed lines indicate the phase speeds (C_r) and the greyed zone identifies conditions leading to the growth of the TS waves.
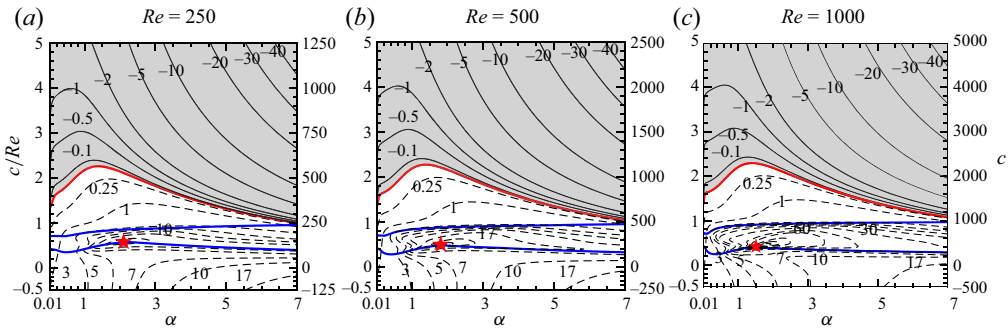

Figure 12. Variations of the pressure gradient correction $B_{norm} = B_{mod}/2\,Re\,A^2$ as a function of α and c for $Re = 250, 500, 1000$ (panels *a–c*, respectively). Solid and dashed lines represent the negative and positive values. The red colour identifies zero isolines. Zones between the blue lines represent the range of natural frequencies of the OS modes. Greyed zones identify conditions leading to a reduction of pressure losses. Red stars identify conditions leading to a local maximum of B_{norm}.

of pressure losses moves towards faster waves as *Re* increases and that there exists the least effective wavenumber α ($\alpha \approx 1.5$) for reduction of these losses. We shall refer to waves with $B_{mod} = 0$ as the transition waves and their phase speed as the transition phase speed c_{tr}. Here, B_{mod} decreases with α and c in a regular manner for sufficiently fast and sufficiently short waves, i.e. fast short waves remain the most effective for reducing pressure losses. The border between the reduction and increase of pressure losses (red line in figure 12) is well above $c/Re = 1$ separating subcritical and supercritical waves – all subcritical and some supercritical waves increase losses. The range of natural frequencies presented in the same figure (blue lines in figure 12) does not show a good correlation with c_{tr}.

Waves propagating upstream ($c < 0$) always increase pressure losses; the magnitude of these losses increases for faster waves. Slow waves propagating downstream also increase losses, but only if their speed is not too large, i.e. $c < c_{tr}$. Variations of the magnitude of these losses are not, however, monotonic with c. There are subcritical waves that produce a local maximum of pressure losses (see red stars in figure 12). In general, the characteristics of such waves show a good correlation with the natural flow
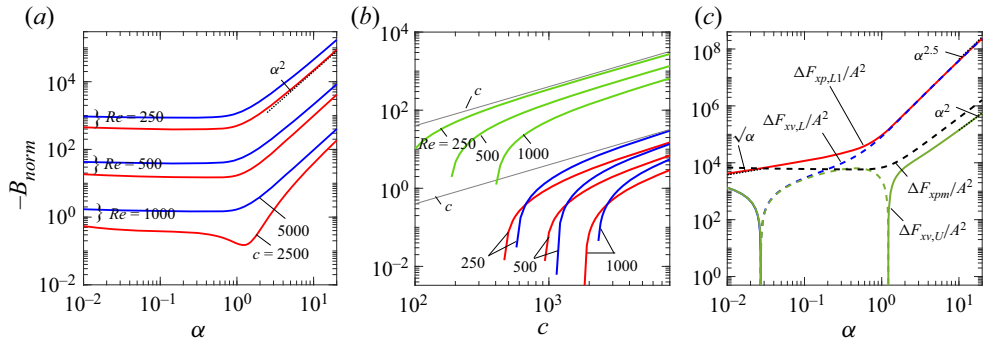
968 A8-19

Figure 13. Variations of the pressure gradient correction $B_{norm} = B_{mod}/2\,Re\,A^2$ (*a*) as a function of α and (*b*) as a function of c ($\alpha = 0.5$, red line; $\alpha = 1.5$, blue line; $\alpha = 30$, green line). Data for $Re = 250,\ 500$ in panel (*a*) were multiplied by 100 and 10, respectively, for display purposes. (*c*) Variations of the modifications of the *x*-components of forces acting on the fluid $\Delta F_{xv,L}/A^2$ (blue line), $\Delta F_{xv,U}/A^2$ (green line) and $\Delta F_{xp,L1}/A^2$ (red line) as functions of α for $Re = 1000$ and $c = 5000(c/Re = 5)$. The solid (dashed) lines correspond to positive (negative) values. The black dashed line illustrates the additional *x*-pressure force $\Delta F_{Xpm}/A^2 = -2B_{mod}/A^2$ generated by the pressure gradient correction.

frequencies. However, conditions corresponding to the local maximum do not correspond to waves that are most likely able to enter into resonance, as there is a mismatch between the wavenumbers and the phase speeds. The waves capable of inducing resonance-like responses are discussed later in this presentation.

Selective cuts through the (α, c)-plane provide details of variations of pressure losses. Here, B_{mod} is nearly independent of α for long waves but begins to increase proportionally to α^2 for $\alpha > 1$, as illustrated in figure 13(*a*). Reduction of losses down to zero is possible if high-speed and extremely short waves are used – these waves are outside of interest in this analysis. Dependence of B_{mod} on c is complex for slow waves, as illustrated in figure 13(*b*) but becomes proportional to c for fast enough waves. The minimum c required for the initiation of the regular, c-proportional growth of B_{mod} varies widely with α and Re; in general, an increase of α reduces the required c. Analysis of results displayed in figure 13(*a,b*) shows that the effectiveness of a specific wave decreases with a rise in Re, similar to slow flows discussed in § 6.1. Increasing wave velocity compensates for the loss of effectiveness.

The interplay between different forces acting on the fluid leading to a reduction of pressure losses is illustrated in figure 13(*c*) for supercritical waves – subcritical waves are discussed later in this presentation. We select the upper end of figure 12(*c*) where B_{mod} varies with c and α in a very regular manner. The pressure force $F_{xp,L1}(= \Delta F_{xp,L1})$ at the vibrating wall reaches a constant in the limit $\alpha \to 0$. Change of viscous force at the lower wall $\Delta F_{xv,L}$ assists with the fluid movement for $\alpha < 0.03$ but opposes this movement for larger α. Change of the viscous force at the upper wall $\Delta F_{xv,U}$ assists fluid movement for $\alpha < 0.03$ and $\alpha > 1.2$, and opposes this movement for the in-between values. Changes in the viscous and pressure forces at the vibrating wall dominate for $\alpha > 3$, where they increase proportionally to $\alpha^{2.5}$. The $\Delta F_{xp,L1}$ is larger than $\Delta F_{xv,L}$ which leads to a reduction of the pressure gradient force $F_{xp,m}$ – this reduction increases proportionally to α^2. Change of the viscous force at the upper wall $\Delta F_{xv,U}$ increases proportionally to α^2 but it plays a marginal role due to its magnitude being significantly smaller than $\Delta F_{xp,L1}$ and $\Delta F_{xv,L}$.
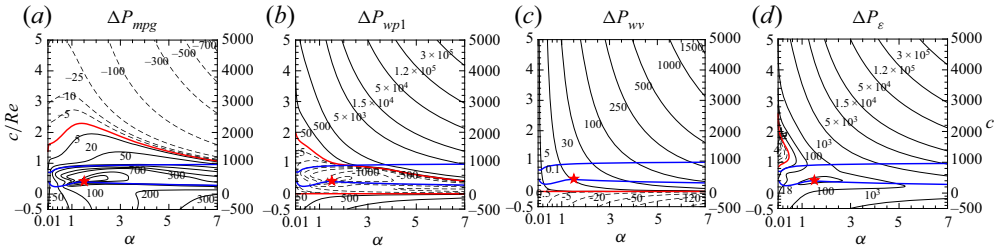
968 A8-20

Figure 14. Variations (*a*) of change in power supplied by the mean pressure gradient ΔP_{mpg}, (*b*) of the work done by the periodic pressure component at the lower wall $P_{wp1}(=\Delta P_{wp1})$, (*c*) of the work done by the viscous forces at the lower wall $P_{wv}(=\Delta P_{wv})$, (*d*) of the increase of the dissipation above the reference dissipation ΔP_{ε} as functions of α and c for $Re = 1000$ and $A = 0.005$. Solid (dashed) lines represent positive (negative) values and the red colour identifies zero isolines. Zones between the blue lines represent the OS modes' natural frequencies. Red stars identify conditions leading to a maximum local increase of B_{norm}.

The qualitative form of energy fluxes remains the same as for smaller *Re*, as demonstrated by comparisons of figures 10 and 14. Supercritical waves deliver most of the power. Most of it is consumed by the increased dissipation leaving only a small fraction available for power reduction, which reduces the amount of energy that has to be supplied by the mean pressure gradient. In contrast, the wall pressure work is negative for subcritical waves, which means that these waves extract energy from the flow. As a result, a significant increase in the pressure gradient is required to maintain the specified flow rate. Such waves produce only a small increase in dissipation (see figure 14). The range of phase speeds increasing pressure losses is much more extensive compared to small *Re* as it includes supercritical waves. Waves leading maximizing losses are marked with a red star.

An unexpected increase in flow resistance caused by subcritical waves can be explained by analysing forces acting on the fluid. Variations of the *x*-component of these forces as functions of α are illustrated in figure 15 for $c/Re = 0.1, 0.5, 2, 5$, which covers the range of c/Re with irregular variations of B_{mod}. The flow resistance in the reference channel is only due to friction. The introduction of vibrations brings in pressure effects and modifies frictional effects. Figure 15(*a*) illustrates forces for waves with $c/Re = 0.1$, which are slower than waves producing a local maximum of losses (see figure 12*c*). Magnitudes of these forces increase monotonically with α, with vibrations increasing friction at the lower wall while reducing friction at the upper wall. Since lower friction is more significant than upper friction, vibrations increase the overall friction. Pressure force opposes fluid movement increasing the mean pressure gradient. An increase of wave speed to $c/Re = 0.5$ leads to non-monotonic variations of all forces with the transition from growth as a function of α to reduction occurring for α between 1.5 and 2 (see figure 15*b*). These conditions correspond to waves producing a local maximum of flow losses. Pressure force at the lower wall opposes fluid movement, with its maximum occurring around $\alpha \approx 1.9$. Viscous force at the lower wall is negligible for $\alpha <\sim 1.4$, but then starts promoting fluid movement reaching a maximum at $\alpha \approx 2$. Viscous force at the upper wall is negligible for $\alpha <\sim 1.4$ but then starts opposing fluid movement reaching a maximum at $\alpha \approx 2$. Overall, viscous forces promote fluid movement for $\alpha >\sim 1.4$. The negative surface pressure force dominates, leading to a significant increase in the required pressure gradient, with its maximum occurring at $\alpha \approx 1.9$. Further increase of wave velocity to $c/Re = 2$ brings us into the zone of supercritical waves, with these waves increasing pressure losses for $\alpha <\sim 3$, but reducing these losses for larger α where variations of B_{mod} as a function of α become very regular (see figure 12*c*). Different forces generally vary in a monotonic manner with an increase of α, as illustrated in figure 15(*c*). Viscous forces oppose fluid
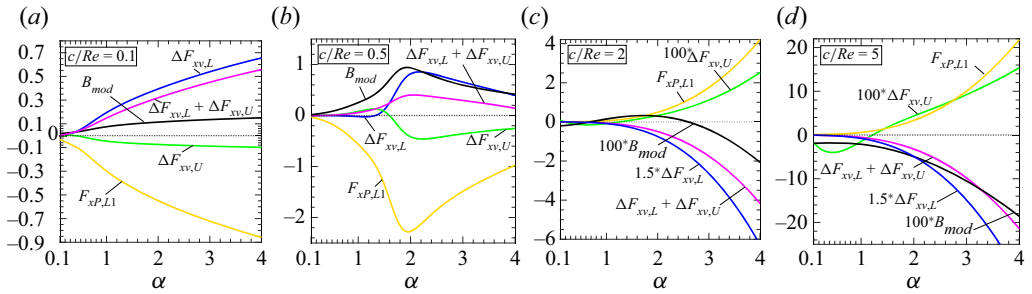
Figure 15. Variations of B_{mod}, $F_{xp,L1}$, $\Delta F_{xv,L}$, $\Delta F_{xv,U}$ and $\Delta F_{xv} = \Delta F_{xv,L} + \Delta F_{xv,U}$ as functions of α for $c/Re = 0.1, 0.5, 2, 5$ in panels (*a–d*), respectively. All results are for $Re = 1000$, $A = 0.005$.

	$\alpha = 0.5$	$\alpha = 1$	$\alpha = 1.5$	$\alpha = 2$	$\alpha = 3$	$\alpha = 5$	$\alpha = 7$
$c/R = 0.1$	-0.120	-0.299	-0.439	-0.548	-0.722	-0.968	-1.122
$c/Re = 0.5$	-0.171	-0.564	-1.358	-2.273	-1.488	-0.520	0.637
$c/Re = 2$	0.013	0.057	0.195	0.489	1.757	8.113	21.216
$c/Re = 5$	0.199	0.578	1.539	3.328	10.027	39.478	95.991

Table 1. Pressure force $F_{xp,L1}$ acting on the fluid at the lower wall ($Re = 1000$, $A = 0.005$).

movement at the lower wall but promote this movement at the upper wall, while pressure forces promotes this movement. It overcomes friction for $\alpha > 2.4$, resulting in a reduction of the required pressure gradient. Waves with $c/Re = 5$ produce regular variations of B_{mod} as a function of α, as illustrated in figure 12(*c*). Generally, viscous forces at the lower wall oppose fluid movement but support this movement at the upper wall. Pressure forces support this movement, reducing the required pressure gradient.

The same data organized by the type of physical quantity and displayed in figure 16 show more vividly how these forces change as the wave speed increases. The magnitudes of all forces increase as wave speed increases up to $c/Re \approx 0.5$. The further increase reverses this trend with the magnitudes of forces decreasing and, eventually, forces changing their direction. A regular pattern is set when c/Re is large enough with force increasing monotonically with c.

The numerical values of the pressure force $F_{xp,L1}$ in table 1 vividly illustrate that this force is directed in the negative x-direction and its magnitude increases monotonically with α for $c/Re = 0.1$. Phase shift, which is discussed later, begins to occur for faster waves ($c/Re = 0.5$), resulting in the initial growth of the magnitude of the pressure force followed by its decrease, but with this force being generally directed in the negative x-direction except for very short waves, e.g. $\alpha = 7$. Waves with $c/Re \geq 2$ create pressure force directed downstream, which increases monotonically with α.

The change in the qualitative character of variations of pressure force with wave speed can be explained by analysing distributions of surface pressure displayed in figure 17(*a–c*) and the x-projection of this pressure onto the wall displayed in figure 17(*d–f*). The force resulting from projection is known as the pressure interaction drag (Mohammadi & Floryan 2012). In the case of 'slow' waves ($c/Re = 0.1$), the position of the 'pressure wave' changes marginally as α increases with its peak located on the upstream side of the wave crest (figure 17*a*). Projection of pressure onto the wall geometry produces x-pressure force whose distribution changes marginally with α, as illustrated in figure 17(*d*), making
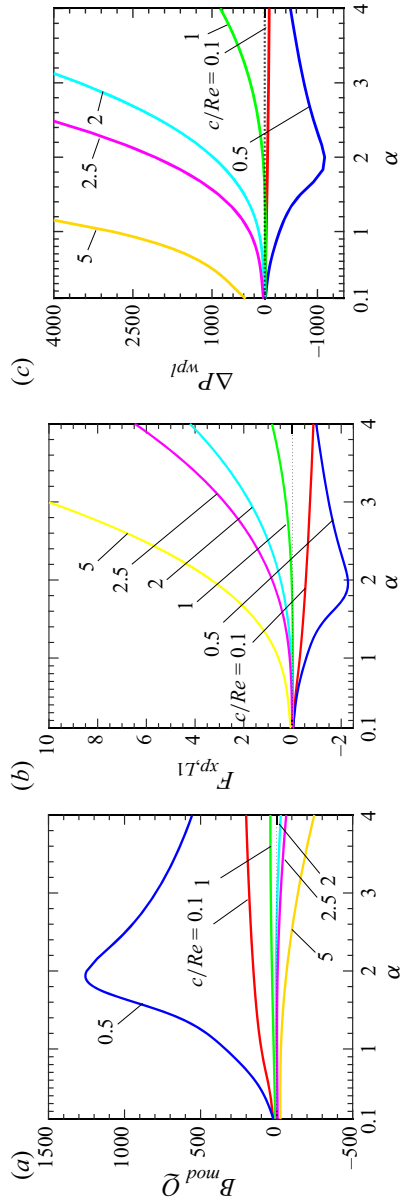
968 A8-22

Figure 16. Variations of the additional power delivered by (*a*) the mean pressure gradient $B_{mod}Q (= \Delta P_{mpg})$, (*b*) the *x*-component of the pressure force at the vibrating wall $F_{xp,L1} (= DF_{xp,L1})$ and (*c*) the work done by the pressure forces at the vibrating wall $P_{wp1} (= \Delta P_{wp1})$ as functions of α for $Re = 1000, A = 0.005$.
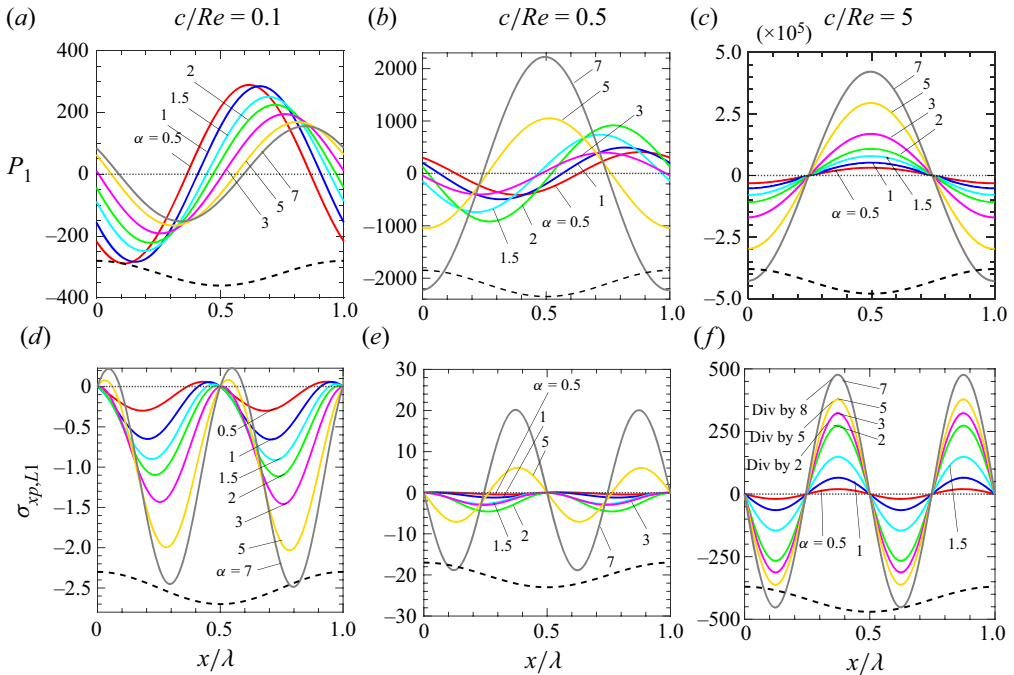
Figure 17. Distributions (*a–c*) of the periodic pressure component p_1 at the lower wall and (*d–f*) of the x-component of force generated by this pressure at the lower wall $\sigma_{xp,L1}$ for $Re = 1000$, $A = 0.005$.

the net pressure force $F_{xp,L1}$ directed upstream. The wave with $c/Re = 0.5$ leads to a phase shift between the 'pressure wave' and the surface wave between $\alpha \approx 2$ and $\alpha \approx 5$ (see figure 17*b*). Long waves have pressure maxima located approximately $\lambda/4$ downstream from the wave trough but short waves have maxima situated at the wave trough. The phase shift changes the projection of pressure onto the surface topography changing the magnitude and direction of the local pressure force (see figure 17*e*) with the net force $F_{xp,L1}$ directed upstream and achieving a maximum at $\alpha \approx 2.0$ – this force is responsible for the local maximum of B_{mod}. The use of fast waves ($c/Re = 5$) fixes the position of the 'pressure wave' to the surface wave with the pressure maximum located at the wave trough (figure 17*c*), and projection of this pressure onto surface geometry loses dependence on α (see figure 17*f*). It produces force directed downstream (see figure 17*d*).

6.3. *Large-Re flows* ($Re \geq 5000$)

An increase of *Re* above 5000 brings in a new effect, i.e. resonance, which we shall discuss later in § 6.3.3. We start the discussion by pointing out that variations of B_{mod} with c and α are, in general, qualitatively similar to variations for smaller *Re* discussed in the previous sections, i.e. fast short waves are the most effective for reducing pressure losses (see figure 18). The minimum speed for waves to be considered 'fast' changes with *Re* as waves with $c > 200$ are 'fast' when $Re = 100$, but waves must reach speed $c > 12\,000$ to become 'fast' when $Re = 6000$. There are notable differences as the range of supercritical waves producing pressure losses increases. The magnitude of pressure losses caused by subcritical waves increases substantially, but there are notable differences. Change with c and α is complex – one can identify waves causing the most significant losses and waves causing the smallest losses. There are two local maxima identified in figure 18 using red
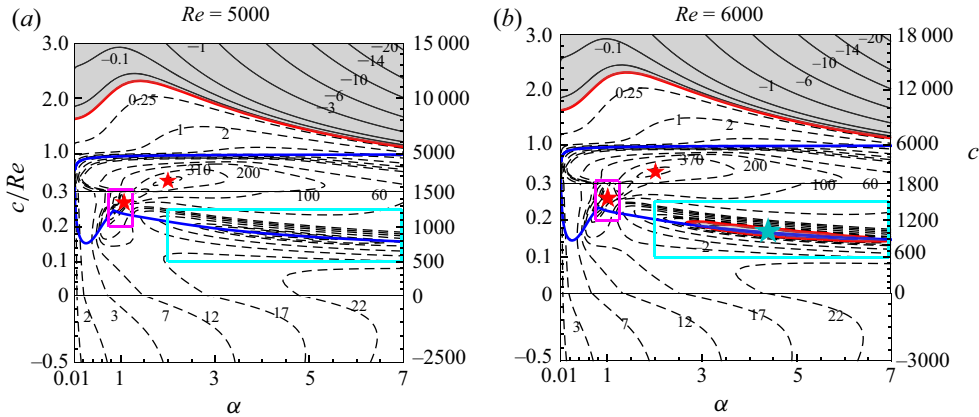
968 A8-24

Figure 18. Variations of the pressure gradient correction $B_{norm} = B_{mod}/2\,Re\,A^2$ as a function of α and c for (*a*) $Re = 5000$ and (*b*) $Re = 6000$. Solid and dashed lines represent the negative and positive values. The red colour identifies zero isolines. Zones between the blue lines represent the range of natural frequencies of the OS modes. Enlargements of pink boxes are displayed in figure 21. Red stars identify conditions leading to a local maximum of B_{norm}. Enlargements of the light blue boxes are displayed in figure 21. Light blue star identifies conditions resulting in the largest reduction of pressure losses by subcritical waves.

stars – the left maximum matches the natural flow frequencies, and the right maximum is associated with a shift of the relative position of the 'pressure wave' and vibration wave discussed in the previous section. There is also a local minimum of B_{mod} which identifies waves producing the lowest increase of pressure losses and, at higher Re, such waves decrease pressure losses. These local minima are marked in figure 18 using light blue stars. The following section provides a discussion of supercritical waves.

6.3.1. *Flow response to supercritical waves*

Variations of pressure losses along selected cuts through the (α, c)-plane are displayed in figure 19. Here, B_{mod} is nearly independent of α for long waves but begins to increase proportionally to α^2 for $\alpha > 1$ (see figure 19*a*), similarly as for flows with smaller Re. Dependence of B_{mod} on c is complex for slow waves, as illustrated in figure 19(*b*), but becomes proportional to c for fast enough waves. The minimum c required for the initiation of the regular, c-proportional growth of B_{mod} varies widely with α and Re; in general, an increase of α reduces the required c. Results displayed in figure 19(*a,b*) demonstrate that the effectiveness of a specific wave decreases with a rise of Re.

Variations of forces acting on the fluid are illustrated in figure 19(*c*) for conditions corresponding to the upper end of figure 18(*b*) where B_{mod} varies with α and c in a regular manner. The pressure force $F_{xp,L1}(= \Delta F_{xp,L1})$ reaches a constant in the limit $\alpha \to 0$ and increases proportionally to $\alpha^{2.5}$ for large α. Change of viscous force at the lower wall $\Delta F_{xv,L}$ opposes fluid movement with this force decreasing to zero for $\alpha \to 0$ and increasing proportionally to $\alpha^{2.5}$ for large α. Change of the viscous force at the upper wall $\Delta F_{xv,U}$ generally opposes fluid movement except for $\alpha > \sim 1.5$, where it supports the fluid movement; it increases proportionally to α^2 for large α. Interplay between $F_{xp,L1}$ and $\Delta F_{xv,L}$ determines the pressure gradient reduction at large α and leads to a reduction of the pressure gradient force $F_{xp,m}$ proportional to α^2. An interplay between $\Delta F_{xv,L}$, $\Delta F_{xv,U}$ and $\Delta F_{xp,L1}$ for small α determines $F_{xp,m}$ in this limit, with $F_{xp,m}$ approaching a constant with $\alpha \to 0$.
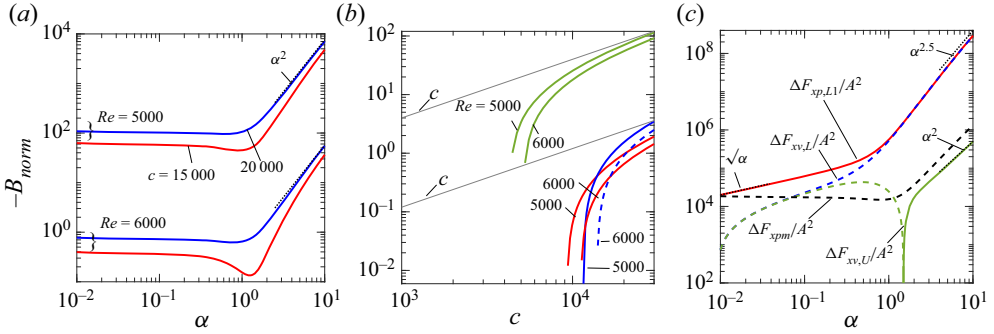
Figure 19. Variations of the pressure gradient correction $B_{norm} = B_{mod}/2\,Re\,A^2$ (*a*) as a function of α and (*b*) as a function of c ($\alpha = 0.5$, red line; $\alpha = 1.5$, blue line; $\alpha = 30$, green line). (*c*) Variations of the modifications of the *x*-components of forces acting on the fluid $\Delta F_{xv,L}/A^2$ (blue line), $\Delta F_{xv,U}/A^2$ (green line) and $\Delta F_{xp,L1}/A^2$ (red line) as functions of α for $Re = 6000$ and $c = 20\,000$. The solid (dashed) lines correspond to positive (negative) values. The black dashed line illustrates the additional *x*-pressure force $\Delta F_{Xpm}/A^2 = -2B_{mod}/A^2$ generated by the pressure gradient correction.
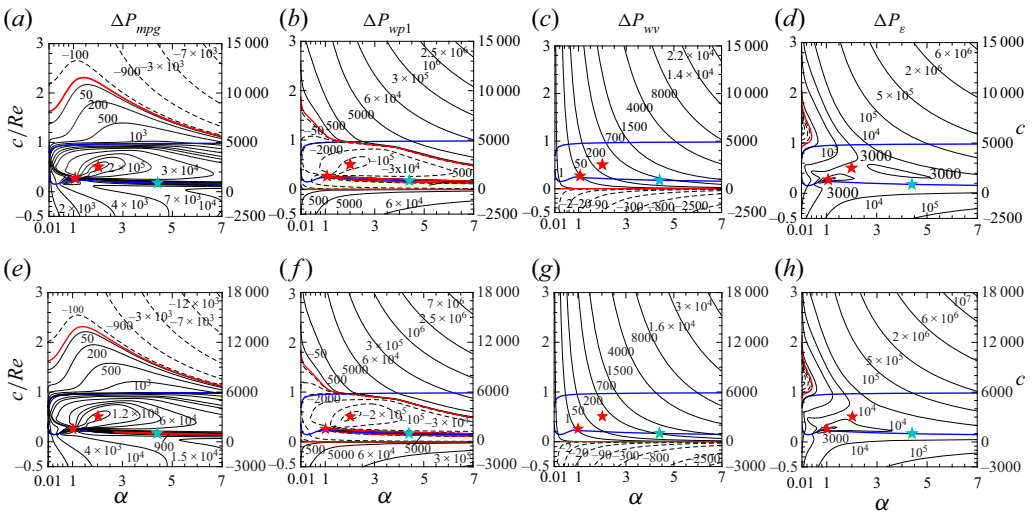

Figure 20. Variations (*a,e*) of change in power supplied by the mean pressure gradient ΔP_{mpg}, (*b,f*) of the rate work done by pressure at the lower wall $P_{wp1}(= \Delta P_{wp1})$, (*c,g*) of the rate of work done by the viscous forces at the lower wall $P_{wv}(= \Delta P_{wv})$, and (*d,h*) of the increase in the dissipation ΔP_ε as functions of α and c/Re. All results are for $A = 0.005$. Panels (*a–d*) display data for $Re = 5000$ and panels (*e–h*) for $Re = 6000$. The solid (dashed) lines represent positive (negative) values. The red colour identifies zero isolines. Zones between the blue lines represent the range of natural frequencies of the OS modes. Red stars identify local conditions leading to a maximum increase of B_{norm}. Blue stars identify conditions resulting in the largest reduction of pressure losses by subcritical waves.

Energy fluxes illustrated in figure 20 are similar to those found for smaller Re. A regular increase of ΔP_{mpg}, ΔP_{wp1}, ΔP_{wv} and ΔP_ε with α and c is observed with the overall energy fluxes being dominated by a balance between dissipation and wall pressure work. Most of the work done by wall pressure increases dissipation, with a small fraction used to reduce pressure losses. The more complex energy fluxes for subcritical waves are discussed in the next section.
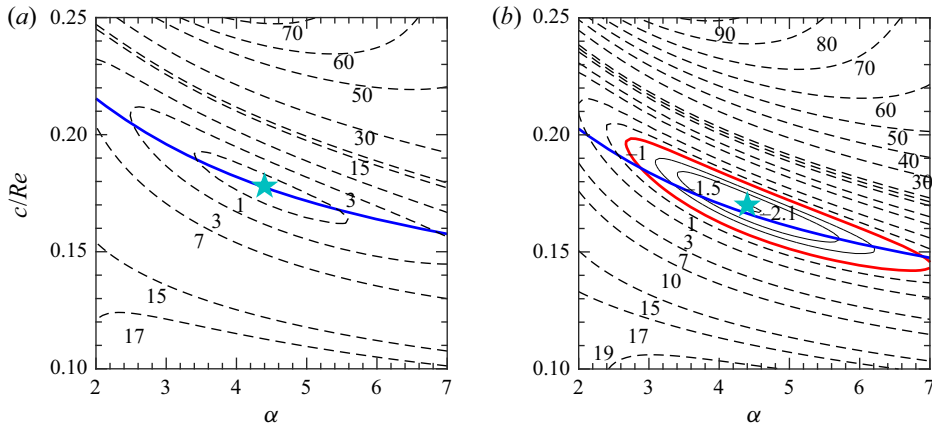
968 A8-26

Figure 21. Variations of the pressure gradient correction $B_{norm} = B_{mod}/2 \, Re \, A^2$ as a function of α and c/Re for $Re = 5000$ and 6000 (panels *a*,*b*, respectively) in the ranges identified by light blue boxes in figure 18. Blue lines represent the lower limit of natural flow frequencies.

6.3.2. *Flow response to subcritical waves away from the resonance*

Results in figure 18 demonstrate intricate changes in the flow response depending on the wavenumber and the phase speed of subcritical waves. Local maxima of pressure losses are identified using red stars and a local minimum is identified using a light blue star. The mechanics of flow response at the upper maximum (upper red star) is the same as discussed in the previous section, i.e. it involves phase change between the vibration wave and the surface pressure. The following section shows that resonance effects are responsible for the lower maximum (lower red star). It remains to explain processes leading to the formation of a local minimum. The discussion is facilitated by replotting in figure 21 variations of B_{mod} in the parameter range identified by light blue boxes in figure 18 – local loss minimum at $Re = 5000$ and local reduction of pressure losses at $Re = 6000$ are visible.

The energy fluxes created by subcritical waves in figure 20 demonstrate that subcritical waves generally lead to negative wall pressure work. The overall energy balance is dominated by an interplay between the wall pressure work and the mean-pressure gradient, with dissipation playing a minor role. The external pressure gradient must increase to overcome the negative wall pressure work to maintain the prescribed flow rate.

Presentation of processes leading to a reduction of pressure losses for specific combinations of α and c identified in figure 18 is facilitated by enlarging the light blue boxes presented in that figure. These enlargements, displayed in figure 22, illustrate intrinsic changes in energy transfers. When $Re = 5000$, the wall pressure work becomes positive, i.e. the wall pressure forces inject energy into the flow, leading to a reduction in the required pressure gradient increase. The level of dissipation changes marginally, and viscous work at the vibrating wall is too small to make a difference. An increase of Reynolds number to $Re = 6000$ amplifies this process with the wall pressure work delivering enough energy to reduce the required mean pressure gradient below the reference level.

The above discussion shows that energy is delivered to the flow by surface pressure work with negligible viscous effect. This energy can be directed into increasing the flow energy (positive pressure work) or extracting energy from the flow (negative work). Most of the positive energy increases dissipation, but some of it may reduce mean pressure gradient requirements. Wave properties determine if vibrations extract energy from the
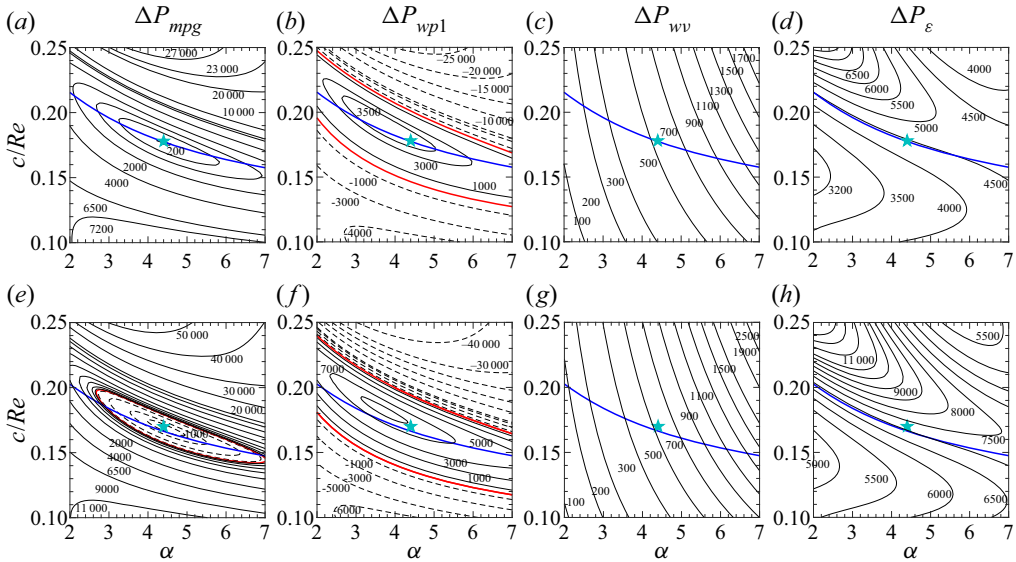
968 A8-27

Figure 22. Variations of the work and power fluxes as functions of α and c/Re for the same parameter range as in figure 21. (*a,e*) Variations of the change in power supplied by the mean pressure gradient ΔP_{mpg}, (*b,f*) the rate of work done by pressure at the lower wall $P_{wp1}(=\Delta P_{wp1})$, (*c,g*) the rate of work done by the viscous forces at the lower wall $P_{wv}(=\Delta P_{wv})$ and (*d,h*) the increase in dissipation ΔP_{ε}. All results are for $A = 0.005$. Panels (*a–d*) display data for $Re = 5000$ and panels (*e–h*) for $Re = 6000$. The solid (dashed) lines represent positive (negative) values. The red colour identifies zero isolines. Blue stars identify conditions resulting in the largest reduction of pressure losses caused by subcritical waves. Blue lines represent the lower limit of natural flow frequencies.

flow or add it to the flow; if energy is added, these properties determine what fraction of pressure work is used to reduce mean pressure gradient requirements. Interestingly, there is a class of subharmonic waves capable of adding enough energy to the flow and directing a sufficiently large part to reduce the pressure gradient below the reference level.

6.3.3. *Flow response to subcritical waves near resonance*

The dynamical properties of the reference flow are characterized by the presence of natural frequencies whose properties are summarized in figure 11 (see also Appendix C). The *y*-symmetry with respect to the channel axis characterizes the spatial distribution of flow modifications associated with natural frequencies in the range of *Re* of interest in this analysis. Vibrations applied at the lower wall produce modifications without such symmetry. We selected two values of *Re*, i.e. 5000 and 6000, for the discussion. The first value is well below the resonance but can create a near resonance, and the second one admits the actual resonance. The waves of interest are identified in figure 18 using pink boxes and variations of B_{mod} within these boxes are displayed in figure 23. Figure 24 displays variations of B_{mod} along cuts through parameter space at a constant *c* and then at a constant α – these cuts are marked in figure 23 using pink crosses. The results show the existence of a small 'ball of influence' in the (α, c)-plane with B_{mod} being negligible outside this 'ball' and increasing exponentially when its centre is approached. The 'ball' becomes narrower and more extreme as *Re* increases from $Re = 5000$ to $Re = 6000$ (see figure 24*a,b*). These results demonstrate that waves with negligible amplitudes, usually irrelevant to flow dynamics, produce significant pressure losses when matching the near-resonance/resonance conditions. The magnitude of response is limited by a mismatch
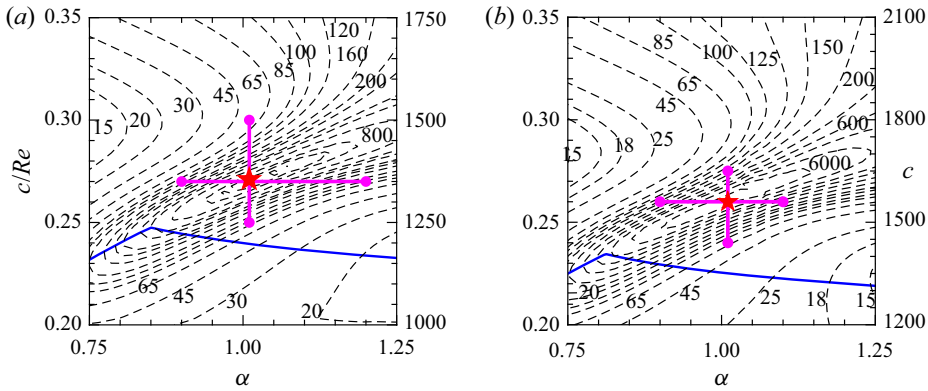
Figure 23. Variations of the pressure gradient correction $B_{norm} = B_{mod}/2\,Re\,A^2$ as a function of α and c for $Re = 5000$, 6000 (panels *a,b*, respectively) in the ranges identified by pink frames in figure 18. Variations of B_{norm} along pink crosses are displayed in figure 22. Blue lines represent the lower limit of natural flow frequencies.

between symmetries of the *y*-symmetric modifications associated with natural frequencies and the no-symmetry of vibration-produced modifications. Overlapping several such curves results in an envelope, which provides means for rapid identification of waves producing a significant flow response (see figure 24*c,d*).

The Reynolds number represents the third axis of the 'ball of influence', whose properties are illustrated in figure 25. A narrow range of *Re* bounded from above and below produces a resonance-type response. The lower bound is evident as the damping of natural frequencies increases with the reduction of *Re*. The upper bound is less obvious, but it is related to a decrease in natural frequencies and a decrease of wavenumbers characterizing resonance when *Re* increases (see figure 11). Data displayed in figure 25(*c*) show that B_{mod} increases proportionally to A^2 even in resonance.

A shift in the most effective vibration wavenumber, as far as initiation of the resonance-type response is concerned, while keeping its phase speed fixed, is illustrated in figure 26. As α decreases from 1.08 to 1.03, *Re* producing a maximum B_{mod} increases from ∼5900 to ∼6100. There is always a range of α and *Re* that initiates a resonance effect. Significant flow response is achieved in this range using extremely small wave amplitudes.

Energy fluxes illustrated in figure 27 show that inserting a minimal amount of wall pressure work creates a significant dissipation which requires a vast increase of pressure gradient to maintain the prescribed flow rate, i.e. vibrations play the role of a catalyst that facilitates energy transfer from the mean pressure gradient into dissipation. It may not be possible to detect such vibrations in actual flows due to their extremely small amplitudes, thus leaving reasons for the observed significant pressure losses unexplained.

6.3.4. *Effects of critical layers*

Critical layers are locations in the flow where the reference flow velocity is equal to the wave velocity. Each subcritical wave forms two critical layers placed symmetrically on both sides of the channel axis whose locations vary between $y = -1$ and $y = 1$ depending on the wave phase speed. As noted in §6.3.2, flow modifications may either extract energy from the reference flow or add energy to this flow. This effect is similar to an instability process where disturbances grow by extracting energy from the flow or decay by returning it to the flow (Schmid & Henningson 2001). An increase of *Re* activates
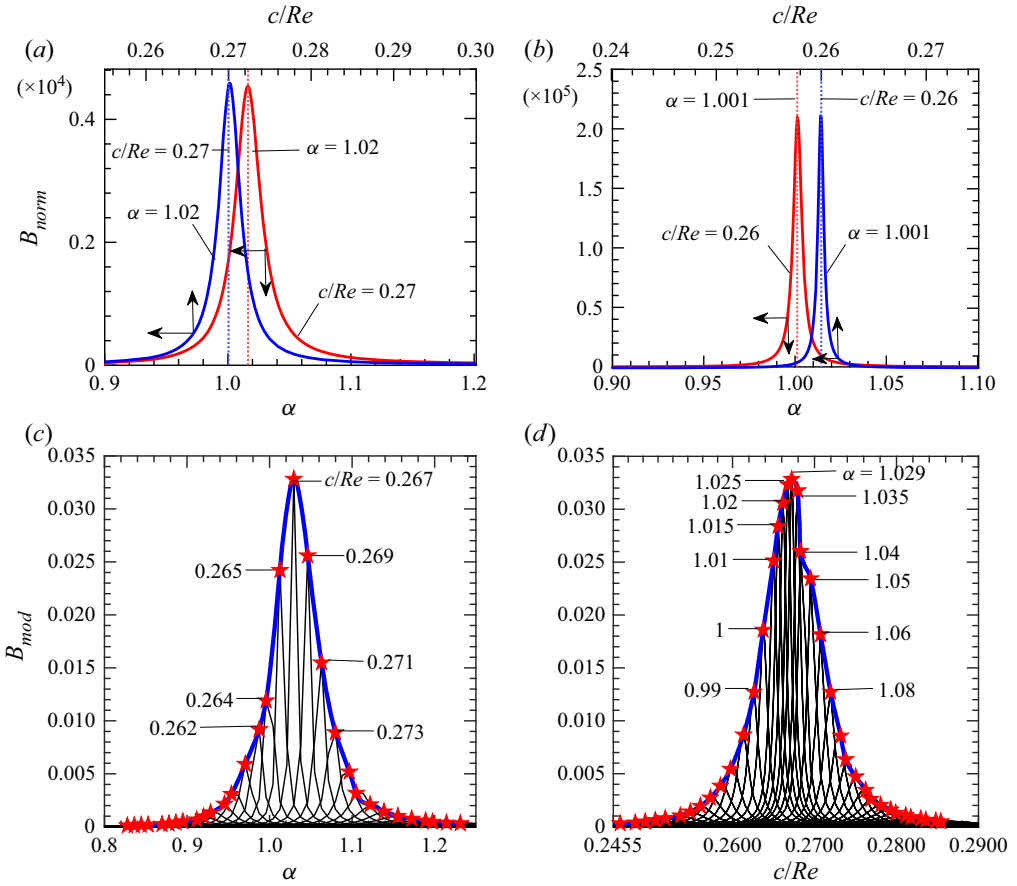
Figure 24. Variations of the pressure gradient correction $B_{norm} = B_{mod}/2\,Re\,A^2$ for $A = 0.00001$ and $Re = 5000,\ 6000$ in panels (a,b), respectively. Flow conditions are marked in figure 23 using pink crosses. Variations of the pressure gradient correction B_{mod} for $A = 0.00001$, $Re = 5500$. Each curve in panels (c,d) corresponds to a different c/Re and a different α, respectively, with the blue curves representing envelopes. Red stars identify the peaks of each curve.
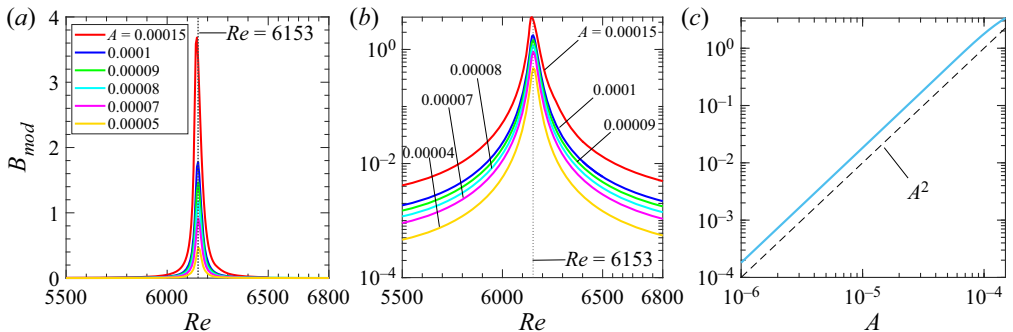

Figure 25. Variations of the pressure gradient correction B_{mod} as a function of Re for $\alpha = 1.01$, $c = 1600$ and different wave amplitudes A displayed using (a) a linear scale and (b) log scale. (c) Variations of B_{mod} as a function of A using the log–log scale for $Re = 6153$, $\alpha = 1.01$, $c = 1600$.
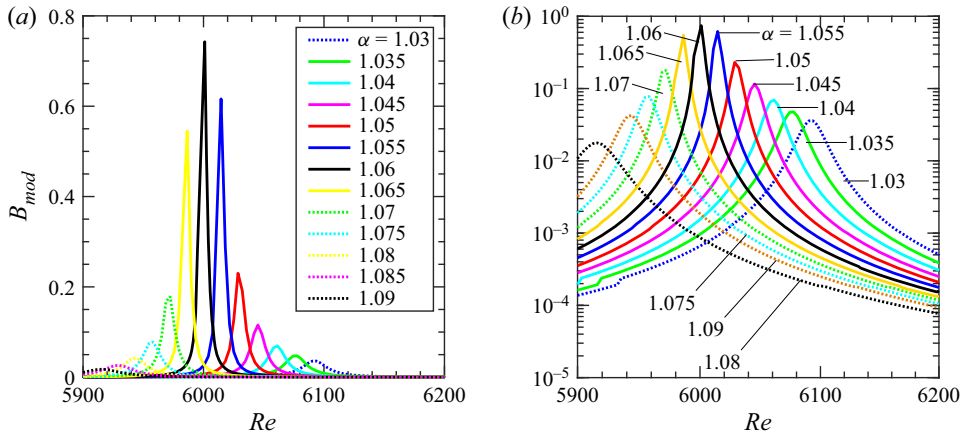
Figure 26. Variations of the pressure gradient correction B_{mod} as a function of Re for $c = 1600$ and selected wavenumbers for $A = 0.00001$. Panel (*a*) uses a linear scale for B_{mod} and panel (*b*) uses a log scale.
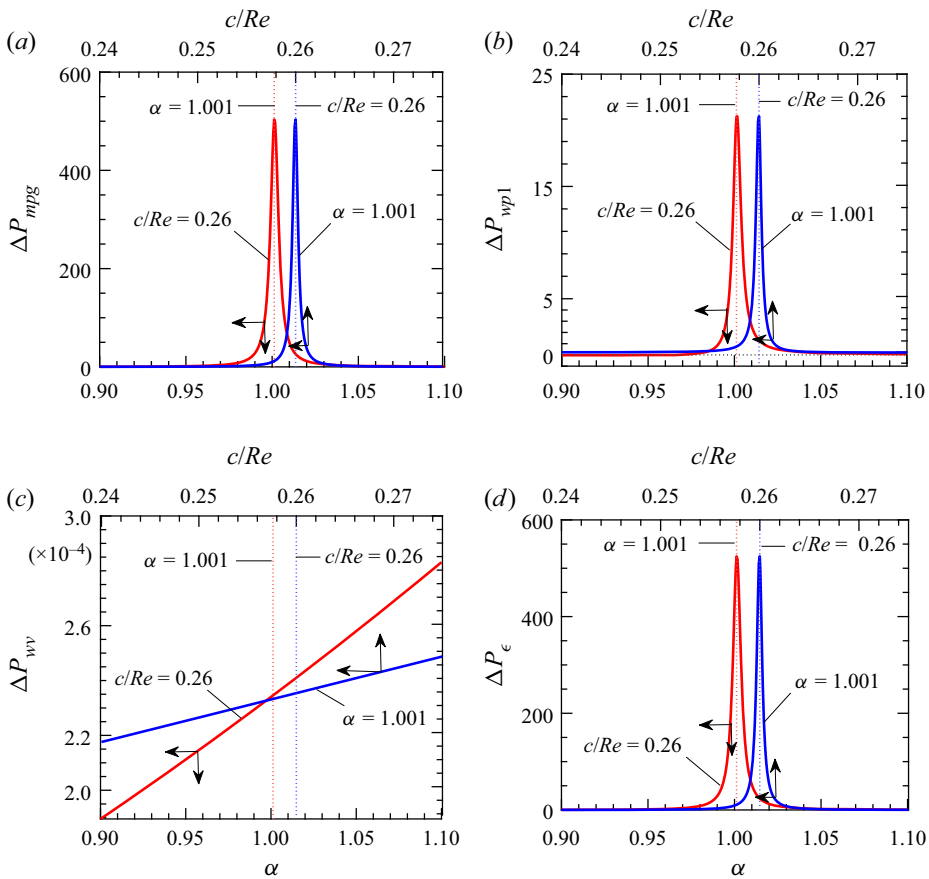

Figure 27. Variations of ΔP_{mpg}, ΔP_{wp1}, ΔP_{wv}, ΔP_{ε} in panels (*a*–*d*), respectively, for $A = 0.00001$ and $Re = 6000$.

the viscous instability mechanism leading to the growth of Tollmien–Schlichting (TS) waves. The essence of this mechanism is that critical layers change phase differences between flow components, enabling energy transfer from the flow to disturbances – the effectiveness of this process increases with *Re*, reaches a maximum, and then decreases. The phase difference generates Reynolds stresses responsible for the energy transfer. There is also an inviscid mechanism, i.e. inflection point instability, but this mechanism is not active in the reference flow (Schmid & Henningson 2001). It remains to investigate if vibrations-created flow modifications create Reynolds stresses whose variations can be correlated with changes in the pressure gradient correction and, thus, to clarify if critical layers play a significant role in the generation of pressure losses as suggested by Hoepffner & Fukagata (2009).

Consider vibration-produced flow modifications induced by small amplitude waves. A semi-analytic solution to this problem is given in Appendix B. Quantities of interest are $\tilde{v}_1$ and $D\tilde{u}_1$ as they combine to produce Reynolds stresses. The global effect of these stresses can be measured by integrating them across the channel, i.e.

$$Rs = \int_{-1}^{1} (\tilde{v}_1^{(1)} D\tilde{u}_1^{(-1)} + \tilde{v}_1^{(-1)} D\tilde{u}_1^{(1)}) \, \mathrm{d}y \qquad (6.10)$$

(see Appendix B for definitions). We select $Re = 6000$ for detailed calculation as critical layers are more effective at larger *Re* and focus on waves producing local minima/maxima of pressure losses. Figure 28 displays variations of *Rs* and the *x*-component of wall pressure force $F_{xp,L1}/A^2$ (see (2.11) for definition). The test conditions are centred at the blue star in figure 18, which corresponds to the local minimum of pressure losses, and at the upper red star, which corresponds to the local maximum. Cuts along fixed α displayed in figure 28(*a*) illustrate the effects of varying wave velocity, which changes the position of critical layers. Local maximum of $F_{xp,L1}/A^2$ correlates well with the local minimum of pressure losses (see solid blue line) and the local minimum correlates well with the local maximum of pressure losses (see solid red line). There is no correlation between variations of *Rs* and local extrema of pressure losses (see red and blue dashed lines), which shows that critical layers do not play a decisive role in creating pressure losses. Cuts along fixed c/Re displayed in figure 28(*b*) demonstrate a good correlation between the local maxima/minima of pressure losses and the wall pressure force and no correlation with variations of *Rs*. These cuts do not change the position of critical layers but change the wave properties. It may be concluded that while phase change between flow components occurs near critical layers, the overall dynamics of this part of the flow field does not dictate variations in flow losses.

7. Conclusions

The effect of surface vibrations on the pressure-gradient-driven flows in channels has been studied to evaluate their resistance mitigation capabilities. Vibrations in the form of travelling waves with prescribed phase speed and amplitude were considered. A detailed analysis has been carried out for laminar flows and monochromatic waves propagating along one of the walls. The effectiveness of vibrations was gauged by determining the pressure gradient correction required to maintain the same flow rate as in the channel without vibrations. The analysis was limited to small wave amplitudes, and the flow Reynolds numbers $Re \leq 6000$ as laminar flows with larger *Re* are subject to various instabilities.

The flow equations were solved in a reference system travelling with the wave. Spatial discretization used Chebyshev expansions in the transverse direction and Fourier
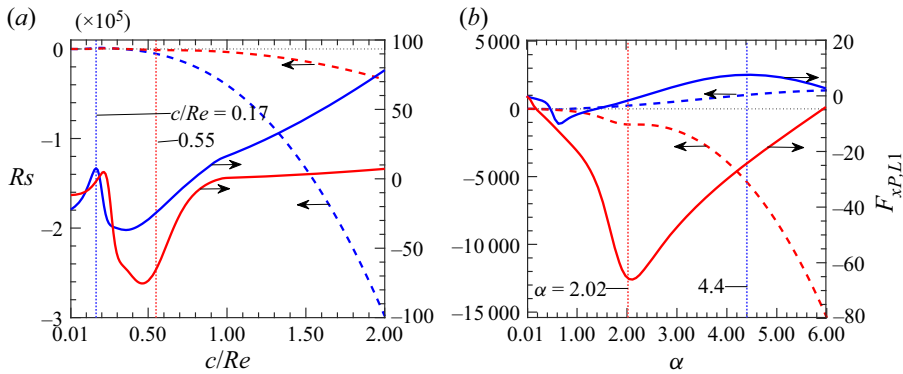
Figure 28. Variations of the Reynolds stress integral Rs (dashed lines) and the x-component of the wall pressure force $F_{xp,L1}$ (solid lines) as functions of (*a*) c/Re and (*b*) α for $A = 0.005$. The remaining conditions correspond to the upper red star (red lines) and blue star (blue lines) in figure 18(*b*). Vertical red and blue dotted lines mark positions of c/Re and α associated with the blue star and the upper red star in figure 18(*b*).

expansions in the streamwise direction combined with the Galerkin projection method. The irregularities of the flow domain were modelled using the immersed boundary conditions (IBC) method. The overall algorithm provided spectral accuracy.

It is shown that waves affect the flow by activating the peristaltic effect. The flow field has similar generic properties over a wide range of parameters. Long waves produce modifications in the form of periodic sloshing penetrating the whole channel. Short waves produce periodic modifications limited to a thin boundary layer adjacent to the vibrating wall. The unmodulated outer flow perceives the edge of the boundary layer as a moving wall. The transition between the sloshing and moving-wall regimes occurs for $\alpha = 0(1)$.

Waves propagating upstream always increase pressure losses, with the magnitude of these losses increasing in a monotonic manner with the wave phase speed and wavenumber. In contrast, the flow response to waves propagating downstream is complex and depends on the flow Reynolds number Re. A loss reduction is possible only if these waves are fast enough with the required minimum speed increasing with Re. Faster waves can be categorized as supercritical, i.e. faster than the reference flow, and subcritical, i.e. waves with velocities similar to the reference flow. In general, supercritical waves reduce pressure losses. The magnitude of this reduction increases monotonically with the wave phase speed and wavenumber but decreases with Re, i.e. wave effectiveness decreases when Re increases. The need for an external pressure gradient is eliminated if sufficiently short and fast waves are used. In general, all subcritical waves decrease pressure losses if $Re <\sim 100$. They increase pressure losses for $Re >\sim 100$, but variations of these losses as a function of the phase speed and wavenumber are irregular and non-monotonic and change with Re. Conditions leading to local maxima and minima of losses at larger Re have been identified. Waves capable of reducing the overall pressure losses have been found for $Re \sim 6000$. Subcritical waves can enter resonance/near-resonance with the natural flow frequencies. It is shown that such waves can produce significant pressure losses even if their amplitudes are negligible.

The energy flows are dominated by a balance between the pressure work at the vibrating wall, the work done by the mean pressure gradient and the dissipation within the fluid volume. When the wall pressure work adds energy to the flow, most of this energy flows to the dissipation with a minor component available to reduce the mean pressure gradient. The mean pressure gradient has to increase significantly when the wall pressure work

extracts energy from the flow. The direction of the wall pressure work can be reversed by changing wave properties.

Funding. This work was carried out with support from NSERC of Canada.

Declaration of interest. The authors report no conflict of interest.

Author ORCIDs.

◉ N.N. Haq http://orcid.org/0000-0002-5934-791X;

◉ J.M. Floryan http://orcid.org/0000-0003-3296-4122.

Appendix A. Long waves

We consider long ($\alpha \to 0$) sinusoidal waves propagating along the lower wall leading to boundary conditions of the form

$$y_U(x) = 1: \quad u = 0, \quad v = 0, \tag{A1a}$$

$$y_L(x) = -1 + \tfrac{1}{2}A\cos(\alpha x): \quad u = 0, \quad v = \tfrac{1}{2}cA\alpha\sin(\alpha x), \tag{A1b}$$

with $A < 4$. The solution domain is regularized using the transformation of the form

$$\xi = \alpha x, \quad \eta = (y - 1)[1 - \tfrac{1}{4}A\cos(\alpha x)]^{-1} + 1, \tag{A2}$$

which maps the original irregular domain into $\eta \in -1, 1$ and introduces a wavelength-based scale in the x-direction leading to the field equations of the form

$$\frac{\partial^2 u}{\partial \eta^2} + [F_1 - F_2(u - c) - F_3 v]\frac{\partial u}{\partial \eta} + F_4\frac{\partial^2 u}{\partial \xi \partial \eta} + F_5\frac{\partial^2 u}{\partial \xi^2} - F_6(u - c)\frac{\partial u}{\partial \xi} - F_6\frac{\partial p}{\partial \xi} - F_2\frac{\partial p}{\partial \eta} = 0, \tag{A3a}$$

$$\frac{\partial^2 v}{\partial \eta^2} + [F_1 - F_2(u - c) - F_3 v]\frac{\partial v}{\partial \eta} + F_4\frac{\partial^2 v}{\partial \xi \partial \eta} + F_5\frac{\partial^2 v}{\partial \xi^2} - F_6(u - c)\frac{\partial v}{\partial \xi} - F_3\frac{\partial p}{\partial \eta} = 0, \tag{A3b}$$

$$\alpha\frac{\partial u}{\partial \xi} + F_7\frac{\partial u}{\partial \eta} + F_8\frac{\partial v}{\partial \eta} = 0, \tag{A3c}$$

$$u(\xi, 1) = 0, \quad v(\xi, 1) = 0, \quad u(\xi, -1) = 0, \quad v(\xi, -1) = \tfrac{1}{2}cA\alpha\sin(\xi), \quad \left(G_1 \int_{-1}^{1} u\,d\eta\right)_{mean} = \frac{8}{3}Re, \tag{A3d–h}$$

with coefficients specified below

$$F_1 = \eta_{xx}G_3^{-1} = \tfrac{1}{4}\alpha^2[-\tfrac{1}{2}G_1 A\cos(\xi) + \tfrac{1}{2}A^2\sin^2(\xi)](\eta - 1) + O(\alpha^4), \tag{A4a}$$

$$F_2 = \eta_x G_3^{-1} = -\tfrac{1}{8}\alpha G_1 A\sin(\xi)(\eta - 1) + O(\alpha^3), \quad F_3 = \eta_y G_3^{-1} = \tfrac{1}{2}G_1 - \tfrac{1}{8}G_1(G_2 - 4) + O(\alpha^4), \tag{A4b,c}$$

$$F_4 = 2\alpha\eta_x G_3^{-1} = -\tfrac{1}{4}\alpha^2 G_1 A\sin(\xi)(\eta - 1) + O(\alpha^4), \quad F_5 = \alpha^2 G_3^{-1} = \tfrac{1}{4}\alpha^2 G_1^2 + O(\alpha^4), \tag{A4d,e}$$

$$F_6 = \alpha\,G_3^{-1} = \tfrac{1}{4}\alpha\,G_1^2 + O(\alpha^3), \quad F_7 = \eta_x = -\tfrac{1}{2}\alpha A(\eta - 1)\sin(\xi)G_1^{-1}, \quad F_8 = \eta_y = 2G_1^{-1}, \tag{A4f–h}$$

$$G_1 = 2 - \tfrac{1}{2}A\cos(\xi), \quad G_2 = 4 + \tfrac{1}{4}\alpha^2 A^2\sin^2(\xi)(\eta - 1)^2, \quad G_3 = \eta_x^2 + \eta_y^2. \tag{A4i–k}$$

The unknowns are represented as expansions of the form

$$(u, v) = (\tilde{u}_0, \tilde{v}_0) + \alpha(\tilde{u}_1, \tilde{v}_1) + O(\alpha^2), \quad p = \alpha^{-1}\tilde{p}_{-1} + \tilde{p}_0 + O(\alpha), \tag{A5a,b}$$

then (A5) is substituted into (A3), and terms of the same orders of magnitude are separated. The resulting sequence of problems begins with the leading-order system being of the form

$$\frac{\partial^2 \tilde{u}_0}{\partial \eta^2} - \frac{1}{2}\, G_1 \tilde{v}_0 \frac{\partial \tilde{u}_0}{\partial \eta} - \frac{1}{4}\, G_1^2 \frac{\partial \tilde{p}_{-1}}{\partial \xi} + \frac{1}{8}\, A \sin(\xi) G_1 (\eta - 1) \frac{\partial \tilde{p}_{-1}}{\partial \eta} = 0, \qquad (A6a)$$

$$\frac{\partial \tilde{p}_{-1}}{\partial \eta} = 0, \quad \frac{\partial \tilde{v}_0}{\partial \eta} = 0, \quad \tilde{u}_0(\xi, \pm 1) = \tilde{v}_0(\xi, \pm 1) = 0, \quad \left(G_1 \int_{\eta=-1}^{\eta=1} \tilde{u}_0 \, d\eta \right)_{mean} = \frac{8}{3} Re. \qquad (A6b\text{--}e)$$

Its solution can be readily determined, i.e.

$$\frac{d\tilde{p}_{-1}}{d\xi} = -16 Re\, G_1^{-3} + 6cA G_1^{-3} \cos(\xi), \quad \tilde{u}_0 = 2Re(1 - \eta^2) G_1^{-1} - \frac{3}{4} cA(1 - \eta^2) \cos(\xi) G_1^{-1}, \quad \tilde{v}_0 = 0. \qquad (A7a\text{--}c)$$

Integration of (A7a) results in an expression for pressure in the form of

$$\tilde{p}_{-1} = -\left(4 + \frac{A^2}{8} \right) Re\, K(\xi) - \frac{1}{2}\, A\, Re \sin(\xi) \left(1 - \frac{A^2}{8} \right)^{-2} G_1^{-2} \left[8 - \frac{A^2}{8} - \frac{3}{2} A \cos(\xi) \right]$$

$$- \frac{c}{4} \left\{ -\frac{9}{4} A^2 K(\xi) + \frac{1}{2} A \sin(\xi) \left(1 - \frac{A^2}{8} \right)^{-2} G_1^{-2} \left[-\frac{3}{4} A^2 - 24 + \frac{1}{2}\, A\, \left(6 + \frac{3}{4} A^2 \right) \cos(\xi) \right] \right\}, \qquad (A8)$$

where

$$K(\xi) = \left(1 - \frac{A^2}{16} \right)^{-5/2} \left\{ \arctan \left[\left(1 + \frac{A}{4} \right)^{1/2} \left(1 - \frac{A}{4} \right)^{-1/2} \tan \left(\frac{\xi}{2} \right) \right] + \pi \frac{\xi + \pi}{2\pi} \right\}. \qquad (A9)$$

In the above, symbol ... stands for the floor function, which has been added to remove spurious discontinuities associated with the arctan function (Jeffrey & Rich 1994), and pressure is normalized with condition $\tilde{p}_{-1}(0) = 0$. To extract the mean pressure gradient, observe that $d\tilde{p}_{-1}/d\xi$ in (4.6a) is an even function of ξ. It can be expressed as a cosine Fourier expansion which can be integrated with respect to ξ term by term to arrive at

$$\tilde{p}_{-1} = \left(1 - \frac{A^2}{16} \right)^{-5/2} \left[-2Re \left(1 + \frac{A^2}{32} \right) + \frac{9}{32} cA^2 \right] \xi$$

$$+ \frac{1}{2} A \left(1 - \frac{A^2}{16} \right)^{-5/2} \left[-3Re + \frac{3}{2} c \left(1 + \frac{A^2}{8} \right) \right] \sin(\xi) + \cdots, \qquad (A10)$$

where the aperiodic term represents the mean pressure gradient $d\tilde{p}_{-1}/d\xi|_{mean}$. The pressure gradient correction can be expressed as

$$B_{mod,a} = Re^2 \frac{dp_0}{dx} - \frac{d\tilde{p}_{-1}}{d\xi} \bigg|_{mean}$$

$$= 2Re \left[-1 + \left(1 + \frac{A^2}{32} \right) \left(1 - \frac{A^2}{16} \right)^{-5/2} \right] - \frac{9}{32} cA^2 \left(1 - \frac{A^2}{16} \right)^{-5/2}. \qquad (A11)$$

The first term on the right-hand side describes the groove effect, which always increases pressure losses, and the second term expresses the wave effect, which reduces losses if the
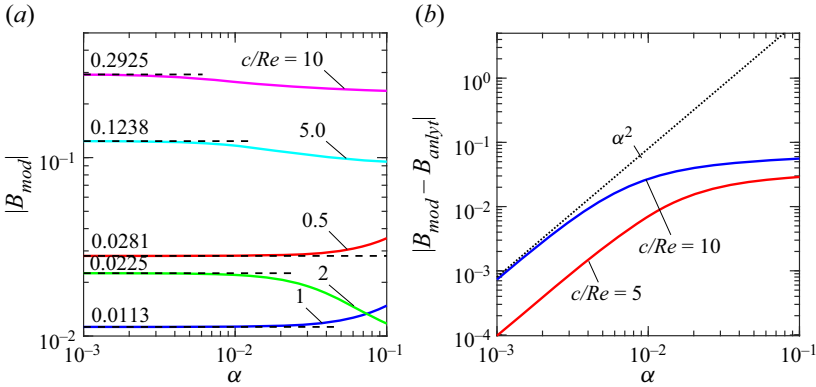
Figure 29. (*a*) Variations of the pressure gradient correction B_{mod} determined numerically and (*b*) the difference between the numerically and analytically determined pressure gradient correction $|B_{mod,n} - B_{mod,a}|$ as functions of α for $A = 0.02$.

wave propagates in the positive *X*-direction. The wave must be fast enough to overcome the groove effect.

The next-order system has the form

$$\frac{\partial^2 \tilde{u}_1}{\partial \eta^2} - \frac{1}{2}\,G_1 \frac{\partial}{\partial \eta}\tilde{v}_1 - \frac{1}{4}\,G_1^2 \frac{\partial \tilde{p}_0}{\partial \xi}$$

$$= -\frac{1}{8}A \sin(\xi)\,G_1(\eta - 1)(\tilde{u}_0 - c)\frac{\partial \tilde{u}_0}{\partial \eta} + \frac{1}{4}\,G_1^2(\tilde{u}_0 - c)\frac{\partial \tilde{u}_0}{\partial \xi}, \qquad (A12a)$$

$$\frac{\partial \tilde{v}_1}{\partial \eta} = \frac{1}{4}A(\eta - 1)\sin(\xi)\frac{\partial \tilde{u}_0}{\partial \eta} - \frac{1}{2}G_1 \frac{\partial \tilde{u}_0}{\partial \xi}, \qquad (A12b)$$

$$\tilde{u}_1(\xi, 1) = 0, \quad \tilde{v}_1(\xi, 1) = 0, \quad \tilde{u}_1(\xi, -1) = 0,$$

$$\tilde{v}_1(\xi, -1) = cA \sin(\xi), \quad \left(G_1 \int_{\eta=-1}^{\eta=1} \tilde{u}_1 \, d\eta\right)_{mean} = 0 \qquad (A12c\text{–}g)$$

and admits only purely periodic solutions.

Comparisons between the numerical ($B_{mod,n}$) and analytical ($B_{mod,a}$) pressure gradient corrections displayed in figure 29 demonstrate that the analytical formula provides a good approximation for $\alpha < 10^{-2}$.

Appendix B. Small amplitude vibrations

We start with the flow (3.2) written in terms of the complete flow quantities

$$(u - c)\frac{\partial u}{\partial x} + v\frac{\partial u}{\partial y} = -\frac{\partial p}{\partial x} + \frac{\partial^2 u}{\partial x^2} + \frac{\partial^2 u}{\partial y^2},$$

$$(u - c)\frac{\partial v}{\partial x} + v\frac{\partial v}{\partial y} = -\frac{\partial p}{\partial y} + \frac{\partial^2 v}{\partial x^2} + \frac{\partial^2 v}{\partial y^2}, \quad \frac{\partial u}{\partial x} + \frac{\partial v}{\partial y} = 0, \qquad (B1a\text{–}c)$$

$$y_U = 1: \quad u = v = 0, \quad y_L = -1 + \frac{1}{2}A\cos(\alpha x): \quad u = 0, \quad v = \frac{1}{2}cA\alpha \sin(\alpha x), \qquad (B1d\text{–}g)$$

$$Q = \left\{ \int_{y_L}^{1} u \, \mathrm{d}y \right\} \bigg|_{mean} = \frac{4}{3} Re. \tag{B1h}$$

The unknowns are represented as expansions in terms of A, i.e.

$$(u, v, \psi) = [\tilde{u}_0, \tilde{v}_0, \tilde{\psi}_0](x, y) + A\, [\tilde{u}_1, \tilde{v}_1, \tilde{\psi}_1](x, y) + A^2[\tilde{u}_2, \tilde{v}_2, \tilde{\psi}_2](x, y) + O(A^3), \tag{B2a}$$

$$p = [B_0 + AB_1 + A^2 B_2 + O(A^3)]x + \tilde{p}_0(x, y) + A\tilde{p}_1(x, y) + A^2 \tilde{p}_2(x, y) + O(A^3), \tag{B2b}$$

then (B2) is substituted into (B1), and terms of the same orders of magnitude are separated. The three leading-order systems have the following form:

$$0(A^0): \frac{\partial^2 \tilde{u}_0}{\partial y^2} + \frac{\partial^2 \tilde{u}_0}{\partial x^2} - (\tilde{u}_0 - c)\frac{\partial \tilde{u}_0}{\partial x} - \tilde{v}_0 \frac{\partial \tilde{u}_0}{\partial y} - B_0 - \frac{\partial \tilde{p}_0}{\partial x} = 0, \tag{B3a}$$

$$\frac{\partial^2 \tilde{v}_0}{\partial y^2} + \frac{\partial^2 \tilde{v}_0}{\partial x^2} - (\tilde{u}_0 - c)\frac{\partial \tilde{v}_0}{\partial x} - \tilde{v}_0 \frac{\partial \tilde{v}_0}{\partial y} - \frac{\partial \tilde{p}_0}{\partial y} = 0, \tag{B3b}$$

$$\frac{\partial \tilde{u}_0}{\partial x} + \frac{\partial \tilde{v}_0}{\partial y} = 0, \tag{B3c}$$

$$0(A^1): \frac{\partial^2 \tilde{u}_1}{\partial y^2} + \frac{\partial^2 \tilde{u}_1}{\partial x^2} - (\tilde{u}_0 - c)\frac{\partial \tilde{u}_1}{\partial x} - \tilde{u}_1 \frac{\partial \tilde{u}_0}{\partial y} - \tilde{v}_0 \frac{\partial \tilde{u}_1}{\partial y} - \tilde{v}_1 \frac{\partial \tilde{u}_0}{\partial y} - B_1 - \frac{\partial \tilde{p}_1}{\partial x} = 0, \tag{B4a}$$

$$\frac{\partial^2 \tilde{v}_1}{\partial y^2} + \frac{\partial^2 \tilde{v}_1}{\partial x^2} - (\tilde{u}_0 - c)\frac{\partial \tilde{v}_1}{\partial x} - \tilde{u}_1 \frac{\partial \tilde{v}_0}{\partial y} - \tilde{v}_0 \frac{\partial \tilde{v}_1}{\partial y} - \tilde{v}_1 \frac{\partial \tilde{v}_0}{\partial y} - \frac{\partial \tilde{p}_1}{\partial y} = 0, \tag{B4b}$$

$$\frac{\partial \tilde{u}_1}{\partial x} + \frac{\partial \tilde{v}_1}{\partial y} = 0, \tag{B4c}$$

$$0(A^2): \frac{\partial^2 \tilde{u}_2}{\partial y^2} + \frac{\partial^2 \tilde{u}_2}{\partial x^2} - (\tilde{u}_0 - c)\frac{\partial \tilde{u}_2}{\partial x} - \tilde{u}_2 \frac{\partial \tilde{u}_0}{\partial x} - \tilde{v}_0 \frac{\partial \tilde{u}_2}{\partial y} - \tilde{v}_2 \frac{\partial \tilde{u}_0}{\partial y} - B_2 - \frac{\partial \tilde{p}_2}{\partial x} = \tilde{v}_1 \frac{\partial \tilde{u}_1}{\partial y} + \tilde{u}_1 \frac{\partial \tilde{u}_1}{\partial x}, \tag{B5a}$$

$$\frac{\partial^2 \tilde{v}_2}{\partial y^2} + \frac{\partial^2 \tilde{v}_2}{\partial x^2} - (\tilde{u}_0 - c)\frac{\partial \tilde{v}_2}{\partial x} - \tilde{u}_2 \frac{\partial \tilde{v}_0}{\partial x} - \tilde{v}_0 \frac{\partial \tilde{v}_2}{\partial y} - \tilde{v}_2 \frac{\partial \tilde{v}_0}{\partial y} - \frac{\partial \tilde{p}_2}{\partial y} = \tilde{v}_1 \frac{\partial \tilde{v}_1}{\partial y} + \tilde{u}_1 \frac{\partial \tilde{v}_1}{\partial x}, \tag{B5b}$$

$$\frac{\partial \tilde{u}_2}{\partial x} + \frac{\partial \tilde{v}_2}{\partial y} = 0. \tag{B5c}$$

Boundary conditions at the upper wall have a simple form, i.e.

$$y = 1: \quad \tilde{u}_0 = \tilde{u}_1 = \tilde{u}_2 = \tilde{v}_0 = \tilde{v}_1 = \tilde{v}_2 = 0. \tag{B6}$$

Boundary conditions at the lower wall are expressed using the boundary conditions transfer procedure, i.e.

$$y = -1: \quad \tilde{u}_0 = \tilde{v}_0 = 0, \tag{B7a}$$

$$\tilde{u}_1 = -\frac{1}{2}\frac{\partial \tilde{u}_0}{\partial y}\cos(\alpha x), \quad \tilde{v}_1 = -\frac{1}{2}\frac{\partial \tilde{v}_0}{\partial y}\cos(\alpha x) + \frac{1}{2}\alpha c \sin(\alpha x), \tag{B7b}$$

$$\tilde{u}_2 = -\frac{1}{2}\frac{\partial \tilde{u}_1}{\partial y}\cos(\alpha x) - \frac{1}{8}\frac{\partial^2 \tilde{u}_0}{\partial y^2}\cos^2(\alpha x), \quad \tilde{v}_2 = -\frac{1}{2}\frac{\partial \tilde{v}_1}{\partial y}\cos(\alpha x) - \frac{1}{8}\frac{\partial^2 \tilde{v}_0}{\partial y^2}\cos^2(\alpha x),$$
$$\tag{B7c}$$

The flow rate constraint is expressed using the stream function in the following form:

$$0(A^0): \ (\tilde{\psi}_0|_{y=1} - \tilde{\psi}_0|_{y=-1})_{mean} = \frac{4}{3}Re, \tag{B8a}$$

$$0(A^1): \ \left(\tilde{\psi}_1|_{y=1} - \tilde{\psi}_1|_{y=-1} - \frac{1}{2}\frac{\partial \tilde{\psi}_0}{\partial y}\bigg|_{y=-1}\cos(\alpha x)\right)_{mean} = 0, \tag{B8b}$$

$$0(A^2): \ \left(\tilde{\psi}_2|_{y=1} - \tilde{\psi}_2|_{y=-1} - \frac{1}{2}\frac{\partial \tilde{\psi}_1}{\partial y}\bigg|_{y=-1}\cos(\alpha x) - \frac{1}{8}\frac{\partial^2 \tilde{\psi}_0}{\partial y^2}\bigg|_{y=-1}\cos^2(\alpha x)\right)_{mean} = 0. \tag{B8c}$$

Solution of (B3), (B6), (B7a) and (B8a) is

$$\tilde{u}_0 = Re \ (1 - y^2), \quad \tilde{v}_0 = 0, \quad \tilde{p}_0 = 0, \quad B_0 = -2Re, \tag{B9}$$

i.e. the flow is not affected by vibrations at the leading order of approximation. The solution of system $0(A)$ can be represented as

$$[\tilde{u}_1, \tilde{v}_1, \tilde{p}_1, \tilde{\psi}_1](x, y) = [\tilde{u}_1^{(1)}, \tilde{v}_1^{(1)}, \tilde{p}_1^{(1)}, \tilde{\psi}_1^{(1)}](y) \, e^{i\alpha x} + [\tilde{u}_1^{(-1)}, \tilde{v}_1^{(-1)}, \tilde{p}_1^{(-1)}, \tilde{\psi}_1^{(-1)}](y) \, e^{-i\alpha x},$$
$$\tag{B10}$$

where $\tilde{u}_1^{(-1)}$, $\tilde{v}_1^{(-1)}$, $\tilde{p}_1^{(-1)}$, $\tilde{\psi}_1^{(-1)}$ are complex conjugates of $\tilde{u}_1^{(1)}$, $\tilde{v}_1^{(1)}$, $\tilde{p}_1^{(1)}$, $\tilde{\psi}_1^{(1)}$. Substitution of (B10) into (B4), separation of Fourier modes, use of (B9), and elimination of $\tilde{u}_1^{(1)}$ and $\tilde{p}_1^{(1)}$ result in the following problem to be solved numerically:

$$D^4\tilde{\psi}_1^{(1)} - [2\alpha^2 + i\alpha(\tilde{u}_0 - c)]D^2\tilde{\psi}_1^{(1)} + [\alpha^4 + i\alpha^3(\tilde{u}_0 - c) - i\alpha D^2\tilde{u}_0]\tilde{\psi}_1^{(1)} = 0, \tag{B11a}$$

$$\tilde{\psi}_1^{(1)}(1) = 0, \quad D\tilde{\psi}_1^{(1)}(1) = 0, \quad \tilde{\psi}_1^{(1)}(-1) = \tfrac{1}{4}c, \quad D\tilde{\psi}_1^{(1)}(-1) = -\tfrac{1}{4}D\tilde{u}_0, \tag{B11b}$$

where $D = \mathrm{d}/\mathrm{d}y$. The reader may note that (B11) represents an inhomogeneous boundary value problem. Its solution is straightforward if the homogeneous problem does not have a non-trivial solution. If this is not the case, the general solution consists of a sum of homogeneous and particular solutions. Non-trivial solutions of the homogeneous problem exist only for certain combinations of parameters (eigenvalue problem), the minimum Reynolds number for the formation of such solutions is $Re = 5772.22$ (Orszag 1971), and all of them are symmetric with respect to the channel centreline for $Re \leq 6000$ which is of interest in this analysis. If non-trivial homogeneous solutions exist, the inhomogeneous

solution must be orthogonal to all of them. All inhomogeneous solutions are asymmetric as only one wall is exposed to vibrations which means that solutions of (B11) exist for arbitrary parameters present in this problem.

Solution of (B11) gives $\tilde{\psi}_1^{(1)}$. The other relevant flow quantities can be determined a posteriori as

$$\tilde{v}_1^{(1)} = -\mathrm{i}\alpha\tilde{\psi}_1^{(1)}, \quad \tilde{u}_1^{(1)} = \frac{i}{\alpha}D\tilde{v}_1^{(1)}, \quad B_1 = 0, \quad \tilde{p}_1^{(1)} = \frac{1}{\alpha^2}D^3\tilde{v}_1^{(1)} - \left[1 + \frac{i}{\alpha}(\tilde{u}_0 - c)\right]D\tilde{v}_1^{(1)} + \frac{i}{\alpha}D\tilde{u}_0\tilde{v}_1^{(1)}.$$

$$(B12a\text{–}d)$$

Solution of system $0(A^2)$ has the form

$$[\tilde{u}_2, \tilde{v}_2, \tilde{p}_2](x, y) = \sum_{n=-2}^{n=2} [\tilde{u}_2^{(n)}, \tilde{v}_2^{(n)}, \tilde{p}_2^{(n)}](y)\,\mathrm{e}^{\mathrm{i}n\alpha x} \qquad (B13)$$

of which only mode zero is on interest. Substitution of (B13) into (B5), (B6), (B7c) and (B8c), and extraction of mode zero leads to the following system:

$$D^2\tilde{u}_2^{(0)} - D\tilde{u}_0\tilde{v}_2^{(0)} - B_2 = \tilde{v}_1^{(1)}D\tilde{u}_1^{(-1)} + \tilde{v}_1^{(-1)}D\tilde{u}_1^{(1)}, \qquad (B14a)$$

$$D^2\tilde{v}_2^{(0)} - D\tilde{p}_2^{(0)} = -\mathrm{i}\alpha\tilde{u}_1^{(1)}\tilde{v}_1^{(-1)} + \mathrm{i}\alpha\tilde{u}_1^{(-1)}\tilde{v}_1^{(1)} + \tilde{v}_1^{(1)}D\tilde{v}_1^{(-1)} + \tilde{v}_1^{(-1)}D\tilde{v}_1^{(1)}, \quad (B14b)$$

$$D\tilde{v}_2^{(0)} = 0, \qquad (B14c)$$

$$y = 1: \quad \tilde{v}_2^{(0)} = 0, \quad \tilde{u}_2^{(0)} = 0, \qquad (B.15a)$$

$$y = -1: \quad \tilde{v}_2^{(0)} = -\tfrac{1}{4}(D\tilde{v}_1^{(1)} + D\tilde{v}_1^{(-1)}), \quad \tilde{u}_2^{(0)} = -\tfrac{1}{4}(D\tilde{u}_1^{(1)} + D\tilde{u}_1^{(-1)}) - \tfrac{1}{16}D^2\tilde{u}_0,$$

$$(B15b)$$

$$\psi_2^{(0)}(1) - \psi_2^{(0)}(-1) = -\tfrac{1}{16}D\tilde{u}_0|_{y=-1}. \qquad (B15c)$$

It can be shown that $\tilde{v}_2^{(0)} = 0$, which leads to a simplified system for the pressure gradient correction:

$$D^2\tilde{u}_2^{(0)} - B_2 = \tilde{v}_1^{(1)}D\tilde{u}_1^{(-1)} + \tilde{v}_1^{(-1)}D\tilde{u}_1^{(1)}, \qquad (B16a)$$

$$\tilde{u}_2^{(0)}(1) = 0, \quad \tilde{u}_2^{(0)}(-1) = -\frac{1}{4}(D\tilde{u}_1^{(1)} + D\tilde{u}_1^{(-1)}) + \frac{1}{8}Re, \quad \int_{-1}^{1} \tilde{u}_2^{(0)}\,\mathrm{d}y = -\frac{1}{8}Re,$$

$$(B16b)$$

with $B_{mod} = -A^2B_2$.

The above analysis shows the existence of two mechanisms of momentum transfer into the fluid. The first one involves periodic modulations which combine at level $0(A^2)$ creating Reynolds stresses (see right-hand side of (B16a)). The second mechanism involves a direct transfer, described by the second condition in (B16b). This condition mimics the slip boundary condition, where the fluid sees the vibrating wall as moving.

Appendix C. Small disturbances in Poiseuille flow

We consider the linear disturbances imposed on the plane Poiseuille flow. Velocity distribution of the flow scaled with the half-channel width and the maximum velocity
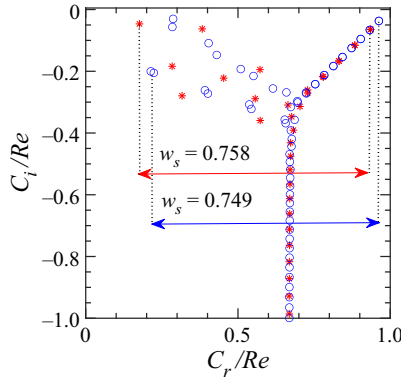
Figure 30. Spectra of the Orr–Sommerfeld problem for $Re = 6000$ and $\alpha = 0.5$ (red stars) and $\alpha = 1.5$ (blue circles). Arrows show the distance between the fastest and slowest waves for a given α.

has the form

$$U(y) = 1 - y^2. \tag{C1}$$

Small disturbances of the form

$$[u_1, v_1, p_1](X, Y, t) = [\hat{u}_1, \hat{v}_1, \hat{p}_1](Y)\, e^{i\delta(X - Ct)} + CC \tag{C2}$$

are added to the flow, and equations are linearized. In the above, CC stands for the complex conjugate, and the complex amplification rate has the form $C = C_r + iC_i$, where C_r stands for the frequency and C_i denotes the amplification rate. Elimination of $\hat{u}_1$ and $\hat{p}_1$ lead to the Orr–Sommerfeld (OS) problem of the form

$$\left.\begin{array}{r}\left[\dfrac{i}{\delta Re}D^4 + \left(\dfrac{-2i\delta}{Re} + U\right)D^2 + \left(\dfrac{i\delta^3}{Re} - D^2U - \delta^2 U\right)\right]\hat{v}_1 = C(D^2 - \delta^2)\hat{v}_1, \\ \hat{v}_1(y = \pm 1) = D\hat{v}_1(y = \pm 1) = 0,\end{array}\right\} \tag{C3}$$

where $D = \mathrm{d}/\mathrm{d}Y$. Equation (C3) represents an eigenvalue problem whose solution gives spectrum C of natural flow frequencies for a specified Re and δ. The problem was converted into a matrix eigenvalue problem by expressing the variable coefficients and unknowns as Chebyshev expansions and constructing algebraic equations for the unknown expansion coefficients using the Galerkin projection method. Boundary conditions were implemented using the Tau procedure (Canuto *et al.* 1992). The spectrum was determined using standard methods (Moler 2004), and the inverse iteration technique was used to improve its accuracy when required (Moradi & Floryan 2014). Typical spectra are displayed in figure 30. The distance w_s between the fastest and the slowest disturbances is marked in some figures in the main text (see, for example, figure 12).

It is known that these disturbances are attenuated for $Re < 5772.22$ (Orszag 1971), so their long-term existence requires continuous energy input from external sources. When $Re > 5772.22$, disturbances grow by extracting energy from the flow. These disturbances are symmetric with respect to the channel axis.

REFERENCES

ABTAHI, A. & FLORYAN, J.M. 2017 Natural convection and thermal drift. *J. Fluid Mech.* **826**, 553–582.
ALI, N., ULLAH, K. & RASOOL, H. 2020 Bifurcation analysis for a two-dimensional peristaltic driven flow of power-law fluid in asymmetric channel. *Phys. Fluids* **32**, 073104.

BEILER, H., ABBAS, A., CHIARAMONTE, J.Y. & SAWYERS, D. 2006 Flow control for aircraft performance enhancements. Overview of Airbus–University cooperation. *AIAA Paper* 2006-3692.

BEWLEY, T.R. 2009 A fundamental limit on the balance of power in a transpiration-controlled channel flow. *J. Fluid Mech.* **632**, 443–446.

CABAL, A., SZUMBARSKI, J. & FLORYAN, J.M. 2001 Numerical simulation of flows over corrugated walls. *Comput. Fluids* **30**, 753–776.

CABAL, A., SZUMBARSKI, J. & FLORYAN, J.M. 2002 Stability of flow in a wavy channel. *J. Fluid Mech.* **457**, 191–212.

CANUTO, C., HUSSAINI, M.Y., QUARTERONI, A. & ZANG, T.A. 1992 *Spectral Methods in Fluid Dynamics*. Springer.

CHEN, Y., FLORYAN, J.M., CHEW, Y.T. & KHOO, B.C. 2016 Groove-induced changes of discharge in channel flows. *J. Fluid Mech.* **799**, 297–333.

FLORYAN, D. 2023 A fundamental limit on energy savings in controlled channel flow, and how to beat it. *J. Fluid Mech.* **954**.

FLORYAN, D. & FLORYAN, J.M. 2015 Drag reduction in heated channels. *J. Fluid Mech.* **765**, 353–395.

FLORYAN, J.M. 1985 Conformal-mapping-based coordinate generation method for channel flows. *J. Comput. Phys.* **58**, 229–245.

FLORYAN, J.M. 1986 Conformal-mapping-based coordinate generation for flows in periodic configurations. *J. Comput. Phys.* **62**, 221–247.

FLORYAN, J.M. 1997 Stability of wall bounded shear layers with simulated distributed surface roughness. *J. Fluid Mech.* **335**, 29–55.

FLORYAN, J.M. 2005 Two-dimensional instability of flow in a rough channel. *Phys. Fluids* **17**, 044101/8.

FLORYAN, J.M. 2007 Three-dimensional instabilities of laminar flow in a rough channel and the concept of a hydraulically smooth wall. *Eur. J. Mech.* (B/*Fluids*) **26**, 305–329.

FLORYAN, J.M., FAISAL, M. & PANDAY, S. 2021 On the peristaltic pumping. *Phys. Fluids* **33**, 033609.

FLORYAN, J.M. & HAQ, H. 2022 Use of vibrations for reduction of resistance in relative movement of parallel plates. *J. Fluid Mech.* **949**, A28.

FLORYAN, J.M., HAQ, H. & BASSOM, A.P. 2023*b* On fast peristaltic waves. *Eur. J. Mech.* (B/*Fluids*) **100**, 239–246.

FLORYAN, J.M. & INASAWA, A. 2021 Pattern interaction effect. *Sci. Rep.* **11**, 14573.

FLORYAN, J.M. & RASMUSSEN, H. 1989 Numerical analysis of viscous flows with free surfaces. *Appl. Mech. Rev.* **42**, 323–341.

FLORYAN, J.M., WANG, W. & BASSOM, A.P. 2023*a* The reduction of pressure losses in thermally-modulated vertical channels. *J. Fluid Mech.* **954**, A38.

FLORYAN, J.M. & ZANDI, S. 2019 Reduction of pressure losses and increase of mixing in laminar flows through channels with long-wavelength vibrations. *J. Fluid Mech.* **864**, 670–707.

FLORYAN, J.M. & ZEMACH, C. 1987 Schwarz-Christoffel transformations – a general approach. *J. Comput. Phys.* **72**, 347–371.

FLORYAN, J.M. & ZEMACH, C. 1993 Schwarz-Christoffel methods for conformal mappings of regions with a periodic boundary. *J. Comput. Appl. Math.* **46**, 77–102.

FUKAGATA, K., SUGIYAMA, K. & KASAGI, N. 2009 On the lower bound of net driving power in controlled duct flows. *Physica* D **338**, 1082–1086.

GATTI, D. & QUADRIO, M. 2016 Reynolds-number dependence of turbulent skin-friction drag reduction induced by spanwise forcing. *J. Fluid Mech.* **802**, 553–582.

GÓMEZ, F., BLACKBURN, H.M., RUDMAN, M., SHARMA, A.S. & MCKEON, B.J. 2016 Streamwise varying steady transpiration control in turbulent pipe flow. *J. Fluid Mech.* **796**, 588–616.

HAN, B.Z. & HUANG, W.X. 2020 Active control for drag reduction of turbulent channel flow based on convolutional neural networks. *Phys. Fluids* **32**, 095108.

HAQ, N.N. & FLORYAN, J.M. 2022 Propulsive effect of wall vibrations. *ASME J. Fluid Engng* **144**, 121204.

HOEPFFNER, J. & FUKAGATA, K. 2009 Pumping or drag reduction. *J. Fluid Mech.* **635**, 171–187.

HOSSAIN, M.Z. & FLORYAN, J.M. 2016 Drag reduction in a thermally modulated channel. *J. Fluid Mech.* **791**, 122–153.

HOSSAIN, M.Z. & FLORYAN, J.M. 2020 On the role of surface grooves in the reduction of pressure losses in heated channels. *Phys. Fluids* **32**, 083610.

HOSSAIN, M.Z., FLORYAN, D. & FLORYAN, J.M. 2012 Drag reduction due to spatial thermal modulations. *J. Fluid Mech.* **713**, 398–419.

HURST, E., YANG, Q. & CHUNG, Y.M. 2014 The effect of Reynolds number on turbulent drag reduction by streamwise traveling waves. *J. Fluid Mech.* **759**, 28–55.

HUSAIN, S.Z. & FLORYAN, J.M. 2008*a* Gridless spectral algorithm for Stokes flow with moving boundaries. *Comput. Meth. Appl. Mech. Engng* **198**, 245–259.

HUSAIN, S.Z. & FLORYAN, J.M. 2008*b* Implicit spectrally accurate method for moving boundary problems using immersed boundary conditions concept. *J. Comput. Phys.* **227**, 4459–4477.

HUSAIN, S.Z. & FLORYAN, J.M. 2010 Spectrally-accurate algorithm for moving boundary problems for the Navier–Stokes equations. *J. Comput. Phys.* **229**, 2287–2313.

HUSAIN, S.Z., SZUMBARSKI, J. & FLORYAN, J.M. 2009 Over-constrained formulation of the immersed boundary condition method. *Comput. Meth. Appl. Mech. Engng* **199**, 94–112.

INASAWA, A., HARA, K. & FLORYAN, J.M. 2021 Experiments on thermal drift. *Phys. Fluids* **33**, 087116.

INASAWA, A., TANEDA, K. & FLORYAN, J.M. 2019 Experiments on flows in channels with spatially distributed heating. *J. Fluid Mech.* **872**, 177–197.

JAFFRIN, M.Y. & SHAPIRO, A.H. 1971 Peristaltic pumping. *Annu. Rev. Fluid Mech.* **3**, 13–37.

JEFFREY, D.J. & RICH, A.D. 1994 The evaluation of trigonometric integrals avoiding spurious discontinuities. *ACM Trans. Math. Softw.* **20**, 124–135.

JIAO, L. & FLORYAN, J.M. 2021*a* On the use of transpiration for reduction of resistance to relative movement of parallel plates. *Phys. Rev. Fluids* **6**, 014101.

JIAO, L. & FLORYAN, J.M. 2021*b* On the use of transpiration patterns for reduction of pressure losses. *J. Fluid Mech.* **915**, A78.

LAUGA, E. 2016 Bacterial hydrodynamics. *Annu. Rev. Fluid Mech.* **48**, 105–135.

LESCHZINER, M. 2020 Friction-drag reduction by transverse wall motion – a review. *J. Mech.* **36**, 649–663.

MAMORI, H., IWAMOTO, K. & MURATA, A. 2014 Effect of the parameters of traveling waves created by blowing and suction on the relaminarization phenomena in fully developed turbulent channel flow. *Phys. Fluids* **26**, 015101.

MIN, T., KANG, S.M., SPEYER, J.L. & KIM, J. 2006 Sustained sub-laminar drag in a fully developed channel flow. *J. Fluid Mech.* **558**, 309–318.

MOHAMMADI, A. & FLORYAN, J.M. 2012 Mechanism of drag generation by surface corrugation. *Phys. Fluids* **24**, 013602.

MOHAMMADI, A. & FLORYAN, J.M. 2013*a* Pressure losses in grooved channels. *J. Fluid Mech.* **725**, 23–54.

MOHAMMADI, A. & FLORYAN, J.M. 2013*b* Groove optimization for drag reduction. *Phys. Fluids* **25**, 113601.

MORADI, H.V. & FLORYAN, J.M. 2013 Flows in annuli with longitudinal grooves. *J. Fluid Mech.* **716**, 280–315.

MOLER, C.B. 2004 *Numerical Computing with MATLAB*. SIAM.

MORADI, H.V. & FLORYAN, J.M. 2014 Stability of flow in a channel with longitudinal grooves. *J. Fluid Mech.* **757**, 613–648.

ORSZAG, S.A. 1971 Accurate solutions of the Orr–Sommerfeld stability equation. *J. Fluid Mech.* **50**, 689–704.

QUADRIO, M. & RICCO, P. 2004 Critical assessment of turbulent drag reduction through spanwise wall oscillations. *J. Fluid Mech.* **521**, 251–271.

QUADRIO, M., RICCO, P. & VIOTTI, C. 2009 Streamwise-travelling waves of spanwise wall velocity for turbulent drag reduction. *J. Fluid Mech.* **627**, 161–178.

RICCO, P., SKOTE, M. & LESCHZINER, M.A. 2021 A review of turbulent skin-friction drag reduction by near-wall transverse forcing. *Prog. Aerosp. Sci.* **123**, 100713.

SCHMID, P.J. & HENNINGSON, D.S. 2001 Stability and transition in shear layer. *Applied Mathematical Sciences*, vol. 142. Springer.

SPALART, P. & MCLEAN, J. 2011 Drag reduction: enticing turbulence, and then an industry. *Phil. Trans. Ser. A Math. Phys. Engng Sci.* **369**, 1556–1569.

SZUMBARSKI, J. & FLORYAN, J.M. 1999 A direct spectral method for determination of flows over corrugated boundaries. *J. Comput. Phys.* **153**, 78–402.

WALSH, M.J. 1983 Riblets as a viscous drag reduction technique. *AIAA J.* **21**, 485–486.

YADAV, N., GEPNER, S.W. & SZUMBARSKI, J. 2021 Determination of groove shape with strong destabilization and low hydraulic drag. *Intl J. Heat Fluid Flow* **87**, 108751.